



Ocean and Sea Ice SAF

Visiting Scientist Report

SAF/OSI/CDOP/KNMI/TEC/TN/168

Near Real-time Sea Ice Discrimination Using SeaWinds on QUIKSCAT

by

M. Belmonte Rivas and A. Stoffelen

(May 2009)

Table of Contents

1 Introduction.....	3
2 SeaWinds on QUIKSCAT.....	4
3 Ocean wind GMF.....	5
4 Sea ice detection	7
4.1 BYU algorithm.....	7
4.2 KNMI algorithm.....	8
5 Algorithm implementation and validation.....	15
5.1 Validation sources – AMSR and BYU SIRF.....	16
5.2 Validation sources – MODIS and ASAR.....	20
5.3 Problems and fixes.....	28
6 Summary and conclusions	44
Appendices.....	45
References.....	50
Acknowledgements	54

1 Introduction

Objective

Within the Ocean and Sea Ice Satellite Application Facility (OSI SAF) created by the European Organisation for the Exploitation of Meteorological Satellites (EUMETSAT), the Royal Netherlands Meteorological Institute (KNMI) has developed sea ice screening routines for both the ERS and ASCAT radar sensors based on probabilistic distances to empirical C-Band models for sea ice and ocean backscatter ([de Haan, 2001], [Verspeek, 2006]).

The Microwave Earth Remote Sensing group at Brigham Young University (BYU) in the United States has also developed an ice screening method for the Ku-Band SeaWinds radar sensor, which KNMI adopted initially for its own processing. Prompted by its own analyses and users queries, the KNMI decided to use an additional Sea Surface Temperature (SST) filter to prevent occasional erratic winds over sea ice surfaces. Since wind information near the ice edge is quite relevant, this document reports on renovated efforts at KNMI to develop an improved sea ice detection algorithm for SeaWinds similar to the one used for ERS and ASCAT sensors, where computed residuals to geophysical Ku-Band ice and ocean model functions are interpreted as probabilities and then combined with prior information on the sea ice state using a Bayesian discrimination algorithm to produce Near Real-Time (NRT) sea ice maps.

2 SeaWinds on QUIKSCAT

The SeaWinds instrument was launched on the QUIKSCAT platform on June 1999 onto a sun-synchronous Low Earth Orbit (LEO) with a period of 101 minutes. SeaWinds uses a rotating dish antenna with two pencil beams that sweep in a circular pattern. The antenna radiates microwave pulses at a frequency of 13.4 GHz and collects the returning backscatter over a continuous 1800 km wide swath, covering 90% of the Earth's surface in one day [Leidner, 2000]. Although the primary mission of QUIKSCAT is to acquire measurements of near-surface winds over the global oceans, other science goals include monitoring the seasonal extent of the Arctic and Antarctic ice packs and the study of changes in rain forest vegetation.

Geometry of observations

SeaWinds employs a single 1 meter parabolic antenna for the reception of horizontal and vertically polarized backscatter with incidence angles of 46 (H-pol) and 54 (V-pol) degrees. The transmitted microwave pulses are frequency chirped and the backscattered returns passed through a Fast Fourier Transform stage to provide sub-footprint range resolution cells ($\sim 25 \times 25 \text{ km}^2$, called slices). Each surface resolution cell (or wind vector cell, WVC) registers a total of four backscatter measurements in sequence, two of them collected by the outer V-pol antenna and another two by the inner H-pol antenna (see Fig.1).

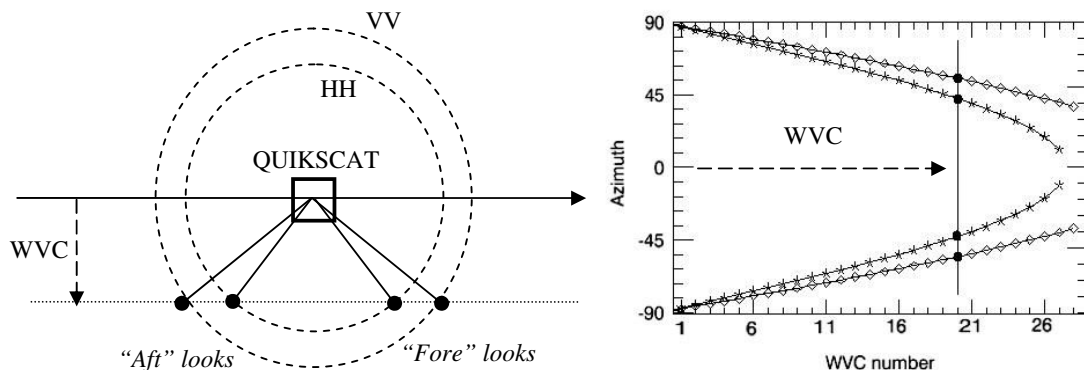


Figure 1 – QUIKSCAT provides a total of four backscatter views per resolution cell

The distance from the sub-satellite to the wind vector cell (i.e. WVC number) determines the azimuthal diversity of the measurement sequence, namely, the arrangement of viewing angles about the surface cell, which should ultimately allow for the detection of the wind direction signature over the ocean.

3 Ocean wind GMF

The empirical Ku-band ocean geophysical model function (GMF) was determined on the basis of a statistical comparison between ADEOS¹ NSCAT 14 GHz dual-polarized backscatter measurements and collocated ECMWF² model winds [Wentz, 1999]. The span of valid model incidence angles ranges from 15 to 65 degrees (55 degrees for H-pol) for wind speeds under 35 m/s. The most salient features of the ocean GMF (see Appendix A) are best described in terms of its own variables, namely radar incidence angle, wind speed and wind direction:

i) *Incidence angle*: the observed values of ocean backscatter at both V and H polarization are equal at nadir and decrease with incidence angle, where V-pol backscatter becomes stronger than H-pol (see Fig.2). This behavior is roughly explained by the physical optics (Kirchhoff) approximation near nadir, and Bragg (resonant) scattering theory at larger incidence angles [Jones, 1977].

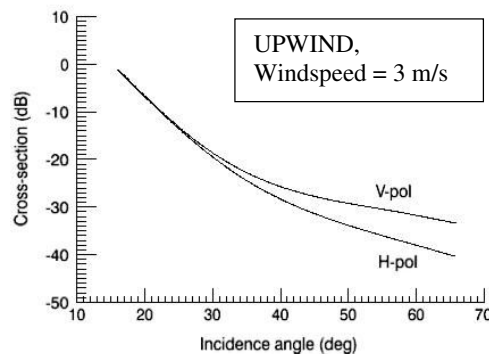


Figure 2 – Ocean backscatter vs radar incidence angle (NSCAT2)

ii) *Wind speed*: The backscatter from the ocean increases with wind speed up to a point of saturation, namely a point beyond which ocean roughness no longer responds to increasing wind speed. Theoretical studies of the ocean wave spectrum [Fernandez, 2006] indicate that the phenomenon of saturation is initiated at the smallest ocean length scales, leaking into larger scales as the wind speed continues to increase. The saturation wind speed is thus expected to increase with radar wavelength and elevation angle (e.g. about 35 m/s for Ku-Band on QUIKSCAT).

iii) *Wind direction*: ocean backscatter shows a double harmonic modulation with respect to wind direction, with a small up/downwind amplitude and a large up/crosswind difference. This azimuthal

¹ ADEOS = Advanced Earth Observing Satellite

² ECMWF = European Center for Medium range Weather Forecasting

anisotropy in backscatter is strongest for moderate winds (~8 m/s) at large incidence angles (see Fig.3), and it vanishes either as wind speeds decrease or approach the backscatter saturation point at 35 m/s.

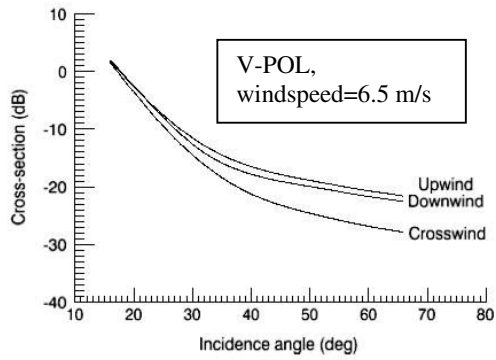


Figure 3a – Ocean backscatter vs. wind direction (NSCAT2)

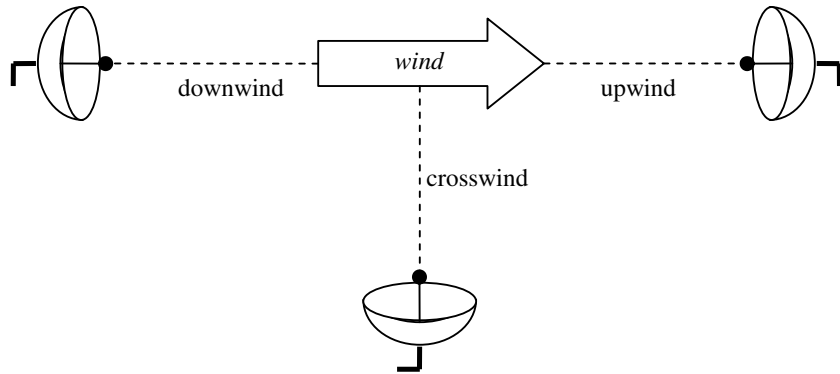


Figure 3b – Wind direction relative to transmit-receive antenna

4 Sea ice detection

In contrast to ocean backscatter, which is a result of surface interaction processes, sea ice backscatter at Ku-band arises from volume interactions deeper in the ice layer. These result in distinct polarization, intensity and directional radiation properties that allow its effective identification against an ocean background. In particular, while ocean (surface) scattering is characterized by steep backscatter gradients relative to the incidence angle and substantial polarization ratios (V/H), volume scattering from sea ice yields smaller gradients and near unity polarization ratios ([Gohin, 1994], [Yueh, 1997]). Also, the azimuthal response of sea ice backscatter is much more isotropic than that of the ocean [Early, 1997].

4.1 *BYU algorithm*

The BYU sea ice detection algorithm is used at NOAA's National Environmental Satellite Data and Information Service (NESDIS) for the operational generation of the SeaWinds Real Time BUFR geophysical products. Following the same principles adopted later by the Norwegian Meteorological Institute [Haarpaintner, 2004] and IFREMER [Ezraty, 2001], the BYU algorithm capitalizes on the contrasting azimuthal and polarization properties of sea ice and ocean backscatter for their effective discrimination ([Remund, 1999] and [Anderson, 2005]). More specifically, the pseudo-polarization ratio ($= \sigma_V/\sigma_H$), mean collected backscatter ($= \sigma_H$), and V and H-pol error standard deviations ($= \Delta\sigma_{H,V}$ or azimuthal variability within a resolution cell) form a 4-dimensional space where ocean and ice clusters are separated. In this transformed space, the BYU algorithm calculates ice/ocean cluster centroids and their covariance matrices to implement maximum likelihood discrimination, using image processing techniques to reduce misclassification noise.

While the BYU algorithm is expected to perform well during calm wind and winter conditions, its seasonal performance has not been validated exhaustively. Some of the problems affecting its accuracy include ([Remund, 1998], [Remund, 2000] and [Abreu, 2002]):

- i) High wind events over the ocean that reduce the ice-seawater contrast, especially in areas of strong cyclonic activity such as the Greenland or Weddell Seas.
- ii) Poorer discrimination over less compact (i.e. lower concentration) ice areas, such as those typical of Antarctica's sea ice margin and the Arctic edge during the melt season.

4.2 KNMI algorithm

For the KNMI sea ice detection algorithm, the former ice/ocean cluster centroids in the transformed space of pseudo-polarization, mean backscatter and azimuthal variability combinations are replaced by empirical model functions for ocean and sea ice backscatter in the original space of backscatter vectors (Fig.4).

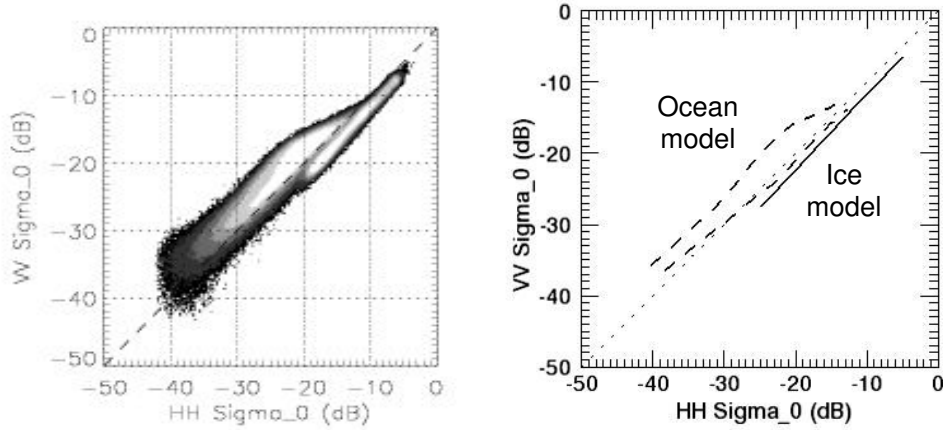


Figure 4 – Observed SeaWinds backscatter distribution (LEFT) vs. empirical model functions (RIGHT)

The KNMI algorithm computes residuals (squared distances) to pre-existing Ku-Band ocean wind and sea ice model functions, and the residuals are converted to probabilities after normalizing by the expected error variance about the corresponding model. These probabilities are finally combined with prior information on the sea ice state using a Bayesian approach to produce daily sea ice maps:

$$p(\text{ice} | \sigma^0) = \frac{p(\sigma^0 | \text{ice}) p_0(\text{ice})}{p(\sigma^0 | \text{ice}) p_0(\text{ice}) + p(\sigma^0 | \text{wind}) p_0(\text{wind})} \quad (1)$$

Where $p(\text{ice} | \sigma^0)$ is the conditional probability of ice given σ^0 measurements, $p(\sigma^0 | \text{ice})$ is the conditional probability of σ^0 given ice (i.e. the distribution of ice backscatter measurements about the ice model), $p(\sigma^0 | \text{wind})$ the distribution of ocean backscatter measurements about the ocean wind model, and $p_0(\text{ice})$ is the *a priori* ice probability. Note that $p_0(\text{wind}) = 1 - p_0(\text{ice})$, since ice and ocean are considered the only two possible outcomes of the algorithm. Observe that modelling the probability distribution of backscatter points about the ocean wind and sea ice models is required, which is what we set out to do next.

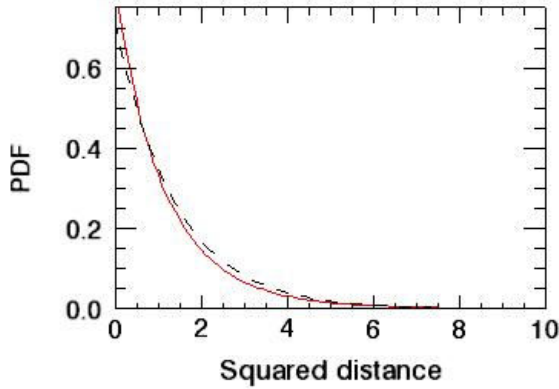
Probability distribution of ocean backscatter $p(\sigma^0 | \text{wind})$

The KNMI SeaWinds Data Processor [de Kloe, 2007] carries all the necessary information about the ocean wind GMF and its expected error variance. This information is embedded in the processor's

normalized maximum likelihood estimator (MLE_{wind}), defined as the squared distance of measurements to the ocean GMF divided by the expected noise variance [Stoffelen, 2006]:

$$MLE_{wind} = \frac{1}{\langle MLE \rangle} \sum_{i=1, \dots, N} \frac{(\sigma_{obs,i}^0 - \sigma_{wind,i}^0)^2}{\text{var}[\sigma_{wind,i}^0]} \quad (2)$$

Where σ_{obs}^0 is the SeaWinds observed backscatter, σ_{wind}^0 is the Ku-band ocean wind GMF (i.e. NSCAT2), N is the number of independent looks available (usually four), $\text{var}[\sigma_{wind}^0]$ is the instrumental noise Gaussian variance [Spencer, 2000] and $\langle MLE \rangle$ is a normalization factor that accounts for deviations from the ocean wind GMF due to geophysical noise effects like sub-cell wind variability [Portabella, 2006]. Note that the normalized MLE_{wind} is constructed to guarantee that the variance of each normalized backscatter component about the ocean wind model is unity (in linear space). Since the normalized MLE_{wind} is expressed as a sum of normally distributed random variables, the probability to find a SeaWinds four-dimensional ocean backscatter vector a squared distance MLE_{wind} away from the two-dimensional ocean GMF surface should be given by a chi-square distribution with two independent degrees of freedom (i.e. an exponential distribution with $L = 2$ [Johnson, 1994], although the exponent of the distribution is empirically adjusted to $L=1.5$, as in Fig.5):



$$p(\sigma^0 | wind) = \frac{1}{L} e^{-MLE_{wind}/L} \quad (3)$$

Figure 5 – Probability distribution of SeaWinds ocean backscatter about the ocean GMF: red is the observed distribution normalized to unit area, and dashed is modeled from Eq. (3) with $L=1.5$

Probability distribution of sea ice backscatter $p(\sigma^0 | ice)$

To obtain the necessary statistical knowledge about the Ku-Band ice model and its error variance, we look at the actual distribution of sea ice backscatter data in the space of SeaWinds measurements. We use good quality, land-masked and rain-free backscatter measurements extracted from the NOAA/NESDIS BUFR files [Leidner, 2000], corrected for two-way atmospheric attenuation using Wentz's SSM/I rain-free climatology and collocated with background BYU sea ice masks (Fig.6).

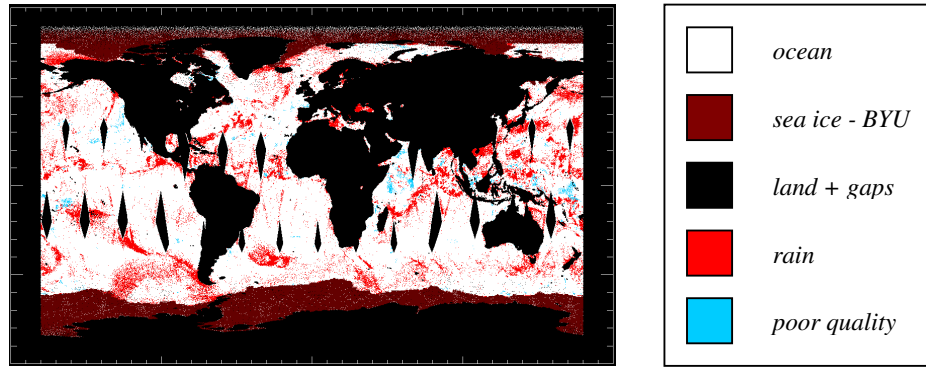


Figure 6 – Daily SeaWinds backscatter measurements

The distribution of sea ice backscatter data in the QUIKSCAT measurement space has been analyzed daily for a period of one year, providing experimental support to the following statements:

- a) Sea ice backscatter distributes along a linear ice model on the QUIKSCAT ‘fore’ and ‘aft’ dB-measurement subspaces (Fig.7)

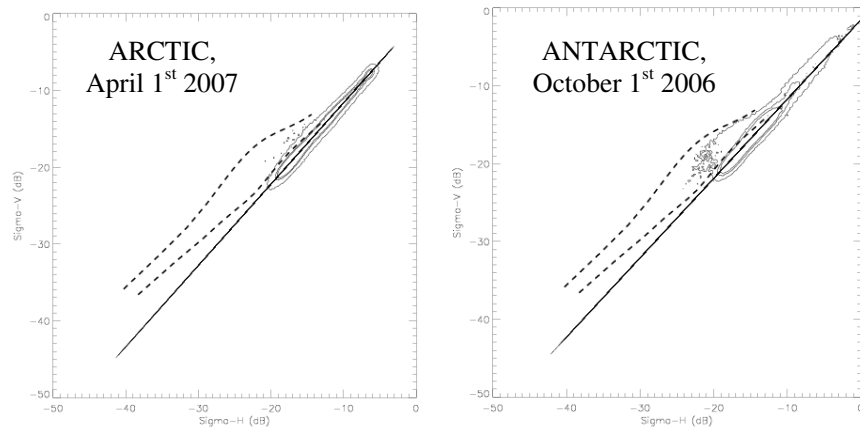


Figure 7 –Histogram (70, 80 and 95%) contours of SeaWinds sea ice backscatter with superimposed *linear ice* and *ocean wind* (NSCAT2, dashed) models

In the *northern hemisphere* (see Appendix B1), the level of sea ice backscatter observed during the winter months is very stable, ranging from -5 to -21 dB for the H-pol component at 46 deg incidence and from -7 to -23 dB for the V-pol component at 54 deg incidence, with little deviation from a straight ice line model. In the summer months, the bright portion of the sea ice distribution (multiyear ice) merges with that of first year ice and a significant number of sea ice backscatter points deviate towards the ocean model (i.e. *mixed ice-water pixels* make appearance). For sea ice that survives the melt season, the transition to multiyear ice is rather abrupt: the backscatter levels of summer ice (from -10 to -20 dB for H-pol at this time of the year) suffer an overall increase of about 5 dB in both the H and V-pol components as the fall season starts, after which new data points start filling the dark portion of the backscatter distribution (new ice production), bringing it

back to its stable winter configuration [Onstott, 1987]. In the *southern hemisphere* (see Appendix B2), most of the sea ice backscatter observed during winter is found between -10 and -20 dB. In contrast to the Arctic case, the brightest portions of the Antarctic backscatter distribution arise from the ice shelves, which also feature larger polarization ratios than multiyear ice. Most of the floating Antarctic ice disappears in the summer, leaving backscatter from ice shelves and mixed ice-water pixels to dominate the distribution of data points. We note that the presence of mixed ice-water pixels is more abundant in the Antarctic than in the Arctic, probably a reflection of the more dynamic environment to which the southern sea ice margin is subject.

A graphical summary of the seasonal dependence of the linear ice model slopes is given in Figure 8 below. The linear model slope is affected by a number of factors, including the presence of mixed ice-water pixels (*MP* in Fig.8 during the austral and boreal summers, negatively biasing the model slope) or backscatter from the ice shelves (late in the austral summer, positively biasing the model slope). To ensure the uniformity of the linear Ku-band sea ice GMF, we take the mean Arctic winter distribution as the most representative of pure ice (volume) backscatter throughout the year and use it for its definition (see Table 1).

Table 1 – Winter sea ice GMF $\sigma_{V,ice}^0 = \sigma_{H,ice}^0 * Slope + Offset$

	Slope	Offset
Arctic Winter	1.06	-1.0 dB

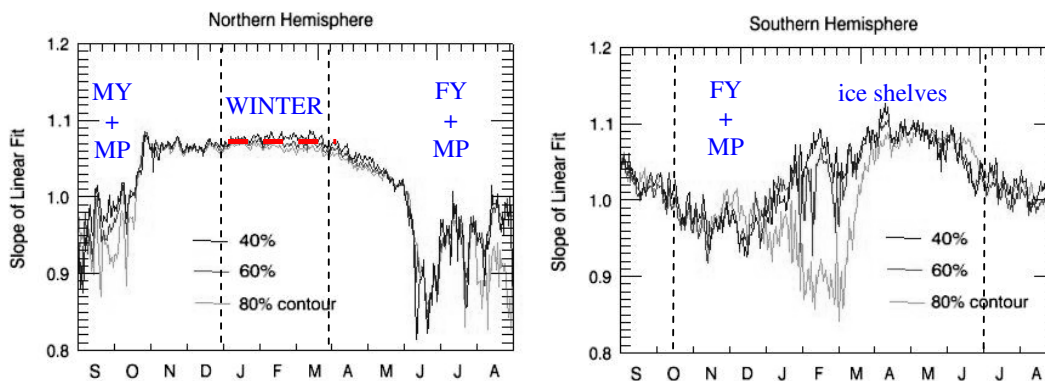


Figure 8 – Daily slopes to linear ice model (Arctic on left and Antarctic on right panel).

The reference Arctic winter slopes are highlighted in red.

- b) The distribution of sea ice backscatter about the winter *linear ice model* is Gaussian

The distribution of sea ice backscatter distances to the linear ice GMF model on the SeaWinds ‘fore’ and ‘aft’ measurement subspaces is Gaussian with a standard deviation of about 0.5 dB

(Fig.9). A summary of the seasonal dependence of the Gaussian fit parameters (standard deviation and biases) for the dispersion of data about the winter linear ice model is given in Figure 10 (see also Appendix C). Observe that the increased dispersion of data in non-winter months mainly relates to the presence of mixed ice-water pixels.

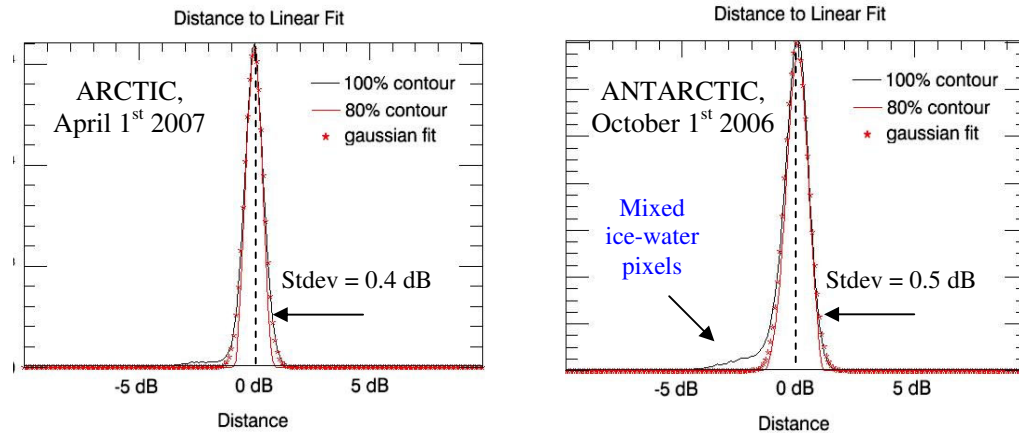


Figure 9 – Histogram of sea ice backscatter distances to linear ice model

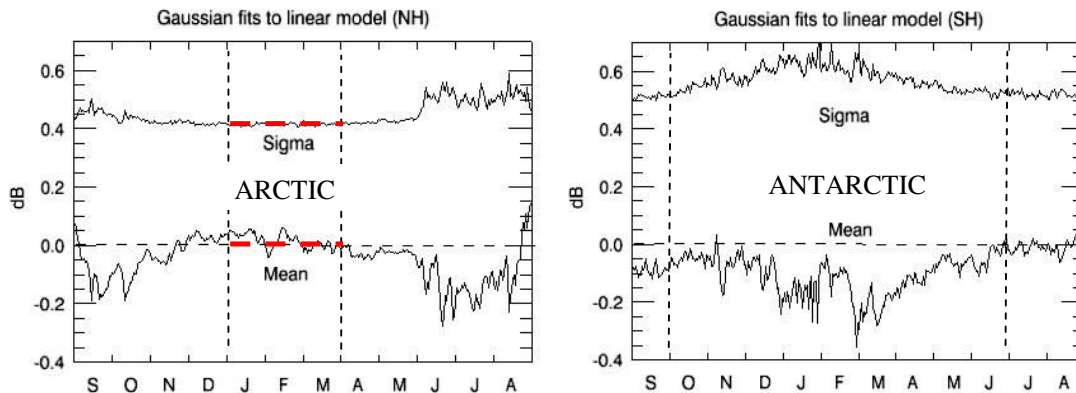


Figure 10 – Gaussian fit parameters (Sigma = Standard deviation; Mean = Bias)

c) Sea ice backscatter is azimuthally isotropic

To measure the degree of azimuthal anisotropy in sea ice backscatter, we calculate the backscatter differences between the aft and fore looks for H and V-polarized components (see Fig. 11). Since the variance of the backscatter differences observed for all azimuths combinations ($\sigma \sim 0.6-0.7$ dB) is roughly equal to twice the variance of the backscatter distance to the linear ice model ($\sigma \sim 0.4-0.5$ dB), we conclude that sea ice backscatter is azimuthally isotropic at Ku-Band. Note that the azimuthal modulation of ocean backscatter can reach up to 6-7 dB, indicating that there is a strong ice-ocean discrimination power encoded in azimuthal variability.

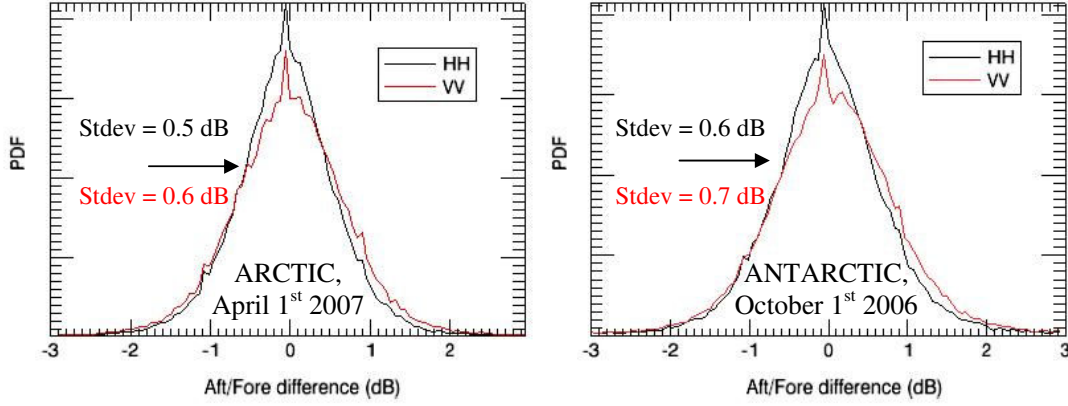


Figure 11a – Azimuthal sea ice backscatter differences ($\Delta\sigma_H^0, \Delta\sigma_V^0$)

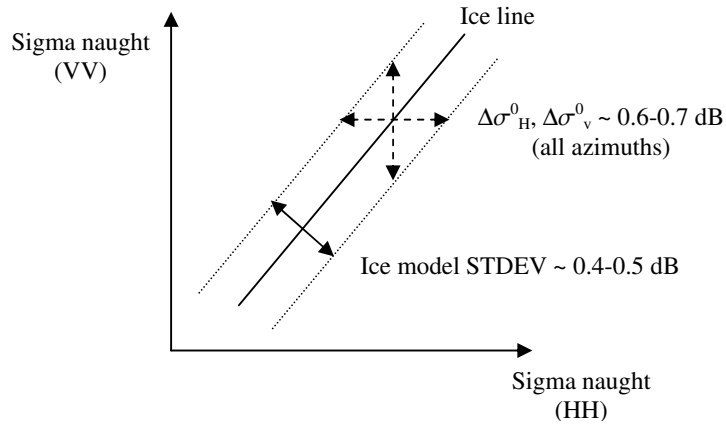


Figure 11b – Azimuthal sea ice backscatter differences (geometry)

So far, we have determined that the variability of sea ice backscatter in the space of SeaWinds measurements appears confined to a linear ice model on H/V polarized components characterized by a Gaussian standard deviation of 0.5 dB (1D). This variability is insensitive to azimuth angle and can be described by a single independent variable which we label ice brightness. Therefore, the formal expression for the conditional probability $p(\sigma^0 | ice)$ to find a SeaWinds four-dimensional sea ice backscatter vector a squared distance MLE_{ice} away from the one-dimensional sea ice GMF line can be modelled by a chi-square distribution with three independent degrees of freedom (see Fig.12) [Johnson, 1994], where:

$$MLE_{ice} = \sum_{i=1, \dots, N} \frac{(\sigma_{obs,i}^0 - \sigma_{ice,i}^0)^2}{\text{var}[\sigma_{ice}^0]} \quad (4)$$

$$p(\sigma^0 | ice) = \sqrt{\frac{MLE_{ice}}{2\pi}} e^{-MLE_{ice}/2} \quad (5)$$

Always as a function of the Gaussian variance of measurements about the linear ice model, $\text{var}[\sigma_{ice}^0]$. The expected dispersion for pure ice backscatter points is given in Table 2 below, which excludes the thin

cloud of *mixed ice-water pixels* that collects on one side of the backscatter distribution (i.e. towards the ocean GMF). Note that the effective detection of mixed ice-water pixels may call for values of $\text{var}[\sigma_{ice}^0]$ larger than those representative of pure ice cells, that is, the definition of sea ice edge can be adjusted by modifying the expected variance of sea ice backscatter about the linear ice GMF.

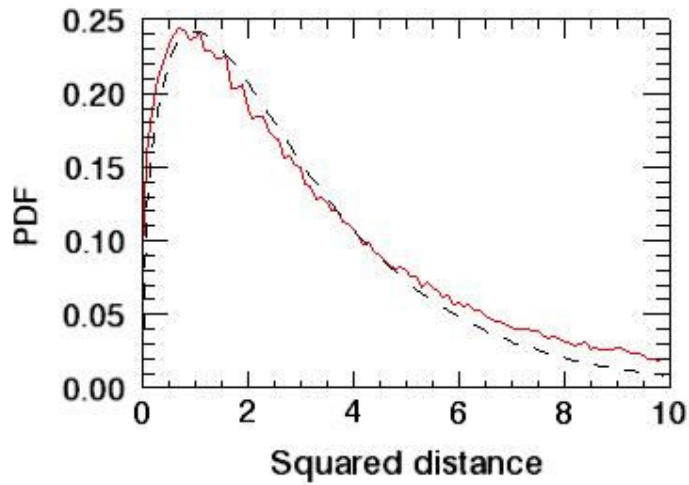


Table 2 – Expected 1-D gaussian scatter about linear sea ice GMF

	Arctic	Antarctic
Std Dev	0.4 dB	0.5 dB

Figure 12 – Probability distribution of sea ice backscatter about the sea ice GMF: red is the observed distribution normalized to unit area, and dashed is modelled from Eq (5).

5 Algorithm implementation and validation

The implementation of the KNMI sea ice detection algorithm using SeaWinds data requires the calculation of the posterior ice probability:

$$p(ice | \sigma^0) = \frac{p(\sigma^0 | ice)p_0(ice)}{p(\sigma^0 | ice)p_0(ice) + p(\sigma^0 | wind)p_0(wind)} \quad (1)$$

where

$$p(\sigma^0 | ice) = \sqrt{\frac{MLE_{ice}}{2\pi}} e^{-MLE_{ice}/2} \quad p(\sigma^0 | wind) = \frac{1}{L} e^{-MLE_{wind}/L} \quad (3) \& (5)$$

and

$$MLE_{wind} = \frac{1}{\langle MLE \rangle} \sum_{i=1, \dots, N} \frac{(\sigma_{obs,i}^0 - \sigma_{wind,i}^0)^2}{\text{var}[\sigma_{wind,i}^0]} \quad MLE_{ice} = \sum_{i=1, \dots, N} \frac{(\sigma_{obs,i}^0 - \sigma_{ice,i}^0)^2}{\text{var}[\sigma_{ice}^0]} \quad (2) \& (4)$$

in terms of the normalized squared distances to the Ku-Band ocean wind and ice GMFs. The local prior probabilities for ice and wind are initially set to $p_0(ice) = p_0(wind) = 0.50$ (reflecting low initial certainty), and then become updated daily using relaxed versions of the previous day posteriors as:

$$p_0(ice) = \begin{cases} 0.50 & \text{if } p(ice | \sigma^0) > 0.30 \\ 0.15 & \text{if } p(ice | \sigma^0) < 0.30 \end{cases} \quad (6)$$

These settings have been chosen after a preliminary trial-and-error study to maximize the level of historic information passed on to the discrimination algorithm, without contradicting the update information carried by new measurements. These processing steps are illustrated in Figure 13 below. In panel A, the distance of backscatter to the ice model is seen to provide a strong ice-water contrast, only disturbed by local structures on the ocean (e.g. see the Bering Sea in Panel A below) that arise from σ^0 -quadruplets lying close to the ice model: these disturbances are most likely caused by rain. In panel B, the distance of backscatter to the ocean wind model also provides a good ice-water contrast, only weakened at extreme high latitudes by the combined effects of a reduced azimuthal diversity in SeaWinds measurements and the presence of bright multiyear ice (which lies close to the high wind speed portion of the ocean model). In panel C, the *a priori* ice probability is built from the sea ice probability map computed for the previous day. The graininess in the raw $p(\sigma^0 | class)$ maps is caused by the SeaWinds daily sampling density in the selected projection grid (i.e. SSM/I polar stereographic, with 12.5 km pixels at 70 deg. latitude).

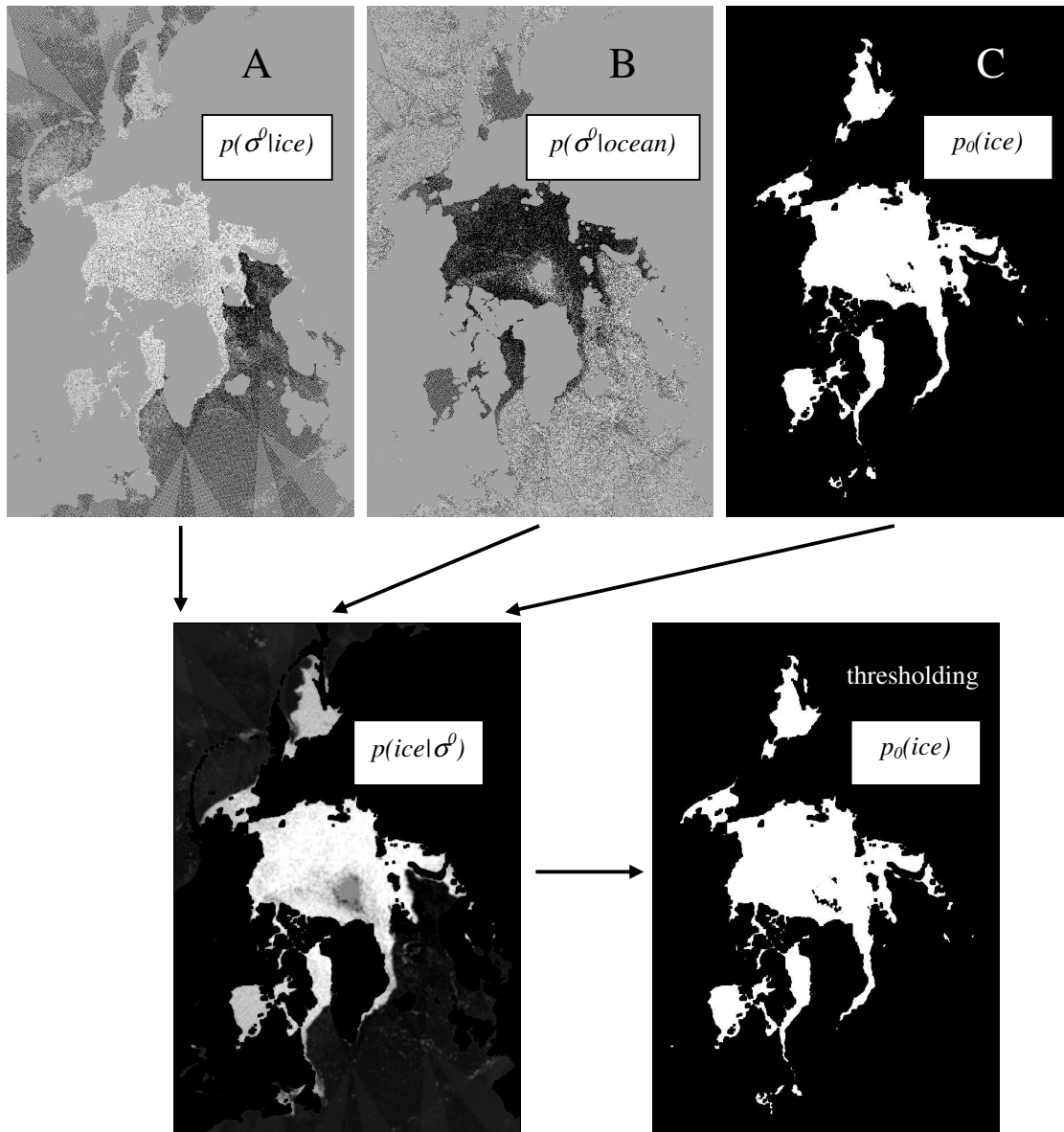


Figure 13 – Bayesian probability combination and thresholding

The SeaWinds KNMI sea ice discrimination algorithm uses a probability threshold of $p(ice|\sigma^o) > 0.45$ for the generation of its sea ice masks.

5.1 Validation sources – AMSR and BYU SIRF

As a primary validation source, we use daily gridded AMSR-E sea ice concentrations from Aqua (AE SI12 v.001 from EOS data gateway, [Cavalieri, 2004]). This 12.5 km sea ice concentration product is generated using the Enhanced NASA Team (NT2) algorithm, which proves accurate to within a 10-15% error against clear sky visible sea ice concentrations ([Meier, 2005], [Cavalieri, 2006]). The wintertime

AMSR (NT2) sea ice extents (15% ice concentration edge [Comiso, 1984]) prove to lie within 10 km of the ice edge extracted from RADARSAT SAR and MODIS image composites [Heinrichs, 2006]. The accuracy of the AMSR (NT2) sea ice concentration algorithm is reported to worsen during the summer months, when it is most affected by weather effects, unresolved thin or low concentration ice types and surface melt effects [Markus, 2000].

As a preliminary exercise, we compare the daily AMSR NT2 sea ice extent estimates against the SeaWinds (QSCAT BYU) sea ice masks included in the NOAA/NESDIS Real Time BUFR Geophysical Data Product during the period spanning from September 15th 2006 through September 15th 2007 (see Fig.14). The comparison is performed on polar 12.5 x 12.5 km² stereographic projection grids with true latitude at 70 degrees, using a common polar-stereo 12.5 km landmask (GSFC II) with a 25 km coastal filter. As additional reference, Figure 14 shows the US National Ice Center (NIC) sea ice extents, which are produced from combined satellite records that include visible, infrared and microwave imagery [Dedrick, 2001]. Caution must be exercised when using NIC charts as a validation source, since they tend to rely heavily on QUIKSCAT and SSM/I imagery.

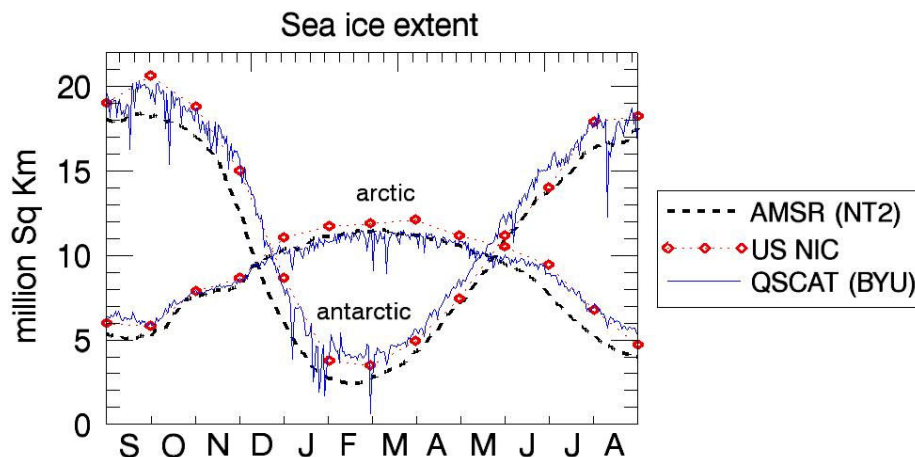


Figure 14 – Daily sea ice extent estimates from AMSR NT2 and SeaWinds Real Time BYU algorithms

Figure 14 shows that the SeaWinds Real Time BYU sea ice masks are rather conservative relative to the passive microwave reference, and that user complaints about erratic winds over sea ice in BUFR products may be associated with occasional glitches in the BYU Real Time masks, which also contain a significant amount of noise along the ice edge [Meier, 2008]. We observe, as noted by [Meier, 2006], that the best agreement between US NIC and AMSR (NT2) sea ice extents is found during the freeze-up period and that US NIC charts tend to overestimate sea ice extents relative to AMSR (NT2) at all other seasons (i.e. see also [Markus, 2002]).

Another source of validation data are the sea ice products derived from SeaWinds backscatter using the threshold-based BYU algorithm on enhanced resolution SIRF images (Scatterometer Image Reconstruction with Filtering, Version 2 from the Scatterometer Climate Record Pathfinder page at <ftp://ftp.scp.byu.edu>, [Remund, 1999]). Unlike the BYU Real Time mask included in the NOAA/NESDIS BUFR products, the BYU SIRF sea ice masks arise from post-processed 36 hour composites of SeaWinds backscatter data. Figure 15 shows that the agreement between the SeaWinds BYU SIRF and the AMSR NT2 algorithms is rather good during the fall and winter months in both hemispheres, providing a robust starting point for the validation of the KNMI Bayesian sea ice detection algorithm. Observe that while earlier work has found general good agreement between microwave active and passive sea ice extents, seasonal discrepancies have been characterized by slightly defective scatterometer extents during the growth season (*winter bias*) and excessive scatterometer extents during the melt season (*summer bias*) ([Remund, 1999] [Meier, 2008]).

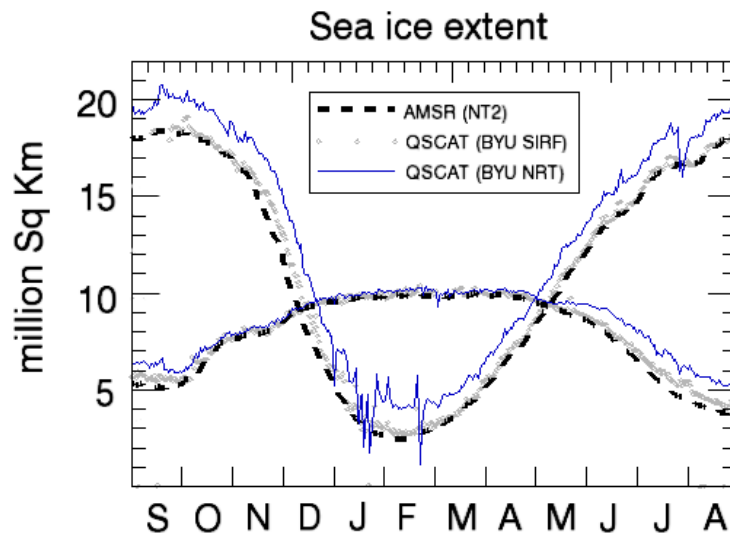


Figure 15 – Daily sea ice extent estimates from AMSR NT2 and SeaWinds BYU algorithms (NRT and SIRF)
(Total areas have been clipped to the limited geographic coverage of BYU SIRF masks)

Figure 16 shows the daily Arctic and Antarctic sea ice extents calculated using the SeaWinds KNMI Bayesian algorithm from September 2006 to September 2007 against the passive microwave AMSR (NT2) reference. The SeaWinds KNMI sea ice extents correspond to three separate runs of the Bayesian algorithm with increasing tolerances for mixed ice/ocean species (i.e. increasing expected variances about the empirical Ku-band ice model, $\text{var}[\sigma_{ice}^0]$). Observe that as the ice model variance increases, the total extent of sea ice detected by the scatterometer increases via the inclusion of a larger number of mixed ice/ocean pixels (i.e. pixels with lower concentration, water saturated and thinner ice species), reducing the winter bias relative to radiometer estimates (i.e. improving the detection of newly formed thin ice during the freeze-up season) but increasing the summer discrepancies (i.e. capturing a larger extension of water saturated and lower concentration ice than the passive microwave technique during the melt season).

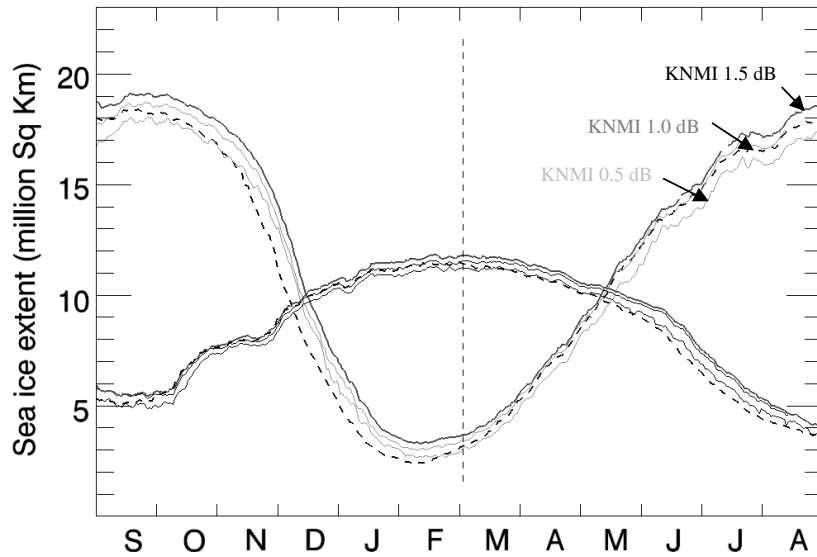


Figure 16 – Tuning the SeaWinds KNMI Bayesian algorithm
 (Dashed line is AMSR NT2, shaded lines are QSCAT KNMI with 0.5, 1.0 and 1.5 dB ice model variances)

In summary, the reported seasonal discrepancies between active (scatterometer) and passive (radiometer) microwave sea ice detection techniques are well reproduced by the KNMI Bayesian algorithm when the tolerance to mixed ice/ocean species is set too low. To improve the detection of rapidly forming ice during the growth season and the characterization of radiometer errors during the summer months, the tolerance to mixed ice/ocean species should be increased up to the point where misclassification noise has not yet become excessive. One such optimal ice model standard deviation is found at 1.5 dB (c.f. Table 2).

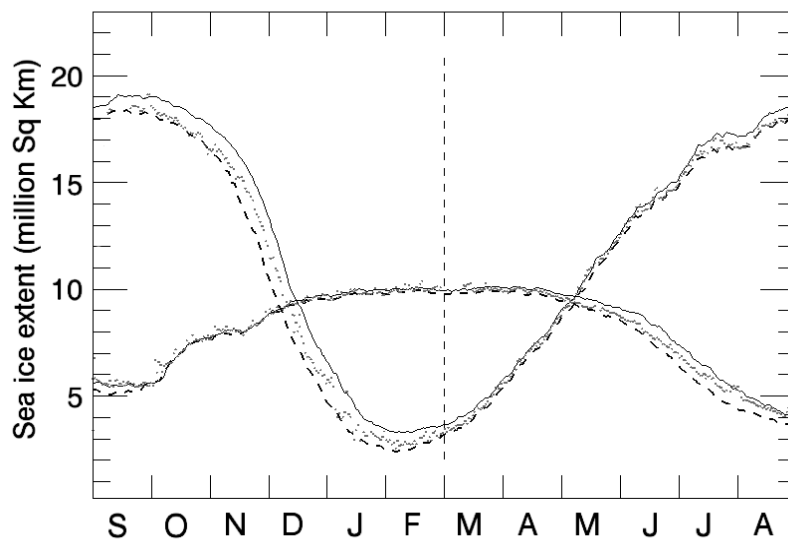


Figure 17 - Daily sea ice extent from SeaWinds KNMI (1.5 dB) algorithm
 (Dashed line is AMSR NT2 and dotted line is SeaWinds BYU SIRF)

Figure 17 shows the evolution of Arctic and Antarctic sea ice extents derived from the AMSR (NT2), QSCAT (BYU SIRF) and QSCAT (KNMI 1.5 dB) algorithms during the 2006/07 freeze-melt cycle. We observe good convergence of all sea ice extent products during the freeze-up months in both hemispheres. Note that the sensitivity of the QSCAT (BYU SIRF) algorithm to stormy wind conditions causes a significant amount of noise during the arctic fall and winter months, which manifests as a large dispersion in daily ice extents. Both active microwave algorithms (KNMI and BYU SIRF) overestimate the spring and summer sea ice extents relative to passive microwaves, but to different degrees. A further look into high resolution optical and radar imagery should help solve this latter ambiguity.

5.2 Validation sources – MODIS and ASAR

While the extensive cloud cover in the polar regions is a factor against the use of optical data for the monitoring of sea ice conditions, the contrast between ice and open water may be unclear for the cloud penetrating SAR due to variable wind conditions at the ice margin. Anyway, the combined use of high resolution optical (MODIS) and synthetic aperture radar (ASAR) data sets compensates for their individual deficiencies and provides a valuable tool for examining algorithm discrepancies over geographically limited areas.

In this section, the KNMI Bayesian sea ice detection algorithm is evaluated against ENVISAT ASAR backscatter and Terra/Aqua MODIS radiance imagery. The MODIS sea ice products (Version 5 MOD29 and MYD29, with 1 km resolution) have been downloaded from the National Snow and Ice Data Center (NSIDC) Distributed Active Archive Center (DAAC). These products are cloud masked and identify sea ice covered oceans by their reflectance characteristics [Riggs, 1999]. The ENVISAT ASAR Global Monitoring data (ASA_GMI_1P, with 1 km resolution) have been provided by the European Space Agency under a Cat-1 PI registration agreement [ASAR, 2007]. ASAR images have been pre-processed on BEAM VISAT software for rough calibration and geo-location.

During the winter months, the ice edge remains a compact boundary between open water and consolidated thick ice. Under these conditions, all three satellite microwave algorithms [AMSR (NT2), QSCAT (BYU SIRF) and QSCAT (KNMI 1.5 dB)] come to agree within ± 2 grid pixels or about 25 km in their determination of the ice edge (Figure 18). The finer spatial resolution of the AMSR (NT2) algorithm allows the radiometer edge to adjust more tightly to the optical/SAR reference and resolve its indentations (Figure 19). The QSCAT (BYU SIRF) algorithm has as fine a spatial resolution as AMSR (NT2), but it is noisier and less reliable. Note that QSCAT (KNMI 1.5 dB) edge stays safely away (~ 25 km or about half the spatial resolution of the SeaWinds footprint) from the least detectable traces of sea ice, providing a rather conservative definition of ice edge but well-suited for masking purposes.

During the growth season, consolidated sea ice progresses behind a rapidly advancing band of newly formed thin ice (frazil, grease ice, nilas, pancake, etc. [Comiso, 1984]). Accurate detection of new ice in active formation areas is difficult because the representativity of daily ice maps degrades rapidly. Besides, scatterometers have been reported to have difficulties in detecting thin ice [Abreu, 2002]. Increasing the KNMI Bayesian ice model variance improves the chances of its detection, but at the cost of increasing the background noise. While the ability of the AMSR (NT2) algorithm to detect thin ice is undisputed, it is closely followed by the QSCAT (KNMI 1.5 dB) algorithm in areas of active ice formation (Figure 20). The QSCAT (BYU SIRF) algorithm shows poorer performance in these cases.

During the melt season and year-round in Antarctica, the ice edge includes lower concentrations of decaying floes with varying amounts of brash (water saturated) ice between them, which are examples of diffuse ice conditions most likely to pass undetected by passive microwave algorithms [Worby, 2004]. Also, ice bands of varying concentration may appear at the Antarctic ice edge at any time of the year. Figures 21-23 illustrate typical detection discrepancies found in the Arctic during the spring and summer months and in the Antarctic all year-round, including low concentrations of decaying floes (Fig. 21), water saturated and brash ice (Fig. 22) and sea ice bands (Fig.23). Note that surface melt effects lead to significant errors in passive microwave estimates. The QSCAT (BYU SIRF) algorithm generally stays midway between the AMSR (NT2) and QSCAT (KNMI 1.5dB) ice edges, and the ability of the QSCAT (KNMI 1.5dB) algorithm to capture diffuse ice remains unmatched. Other problems with the QSCAT (BYU SIRF) algorithm that are overcome by the newer KNMI Bayesian approach, besides the limited geographical coverage and poorer time resolution, is the lack of detection of water openings within the ice pack (polynyas).

In conclusion, we encounter three types of errors when comparing active vs. passive microwave derived sea ice extents. The first relates to the detection of rapidly forming thin ice during the growth season (scatterometer *winter bias*). The second relates to the detection of diffuse ice conditions during the melt season (radiometer *summer bias*), and the last one is related to the presence of misclassified ice patches over the ocean (*ocean noise*). The KNMI Bayesian algorithm has been adjusted so that scatterometer winter biases are minimized without incurring in excessive ocean noise. In this sense, the KNMI Bayesian approach proves superior to the threshold-based BYU SIRF algorithm. The resulting sea ice extents agree with their passive microwave counterparts to within ± 25 km during the fall and winter months, and prove more sensitive to diffuse ice conditions during the melt season (see Figures 25 through 37). The KNMI Seawinds Bayesian algorithm provides a conservative definition of sea ice edge, more in line with that provided by ship observations and well-suited for applications that require reliable masking of sea ice all year round.

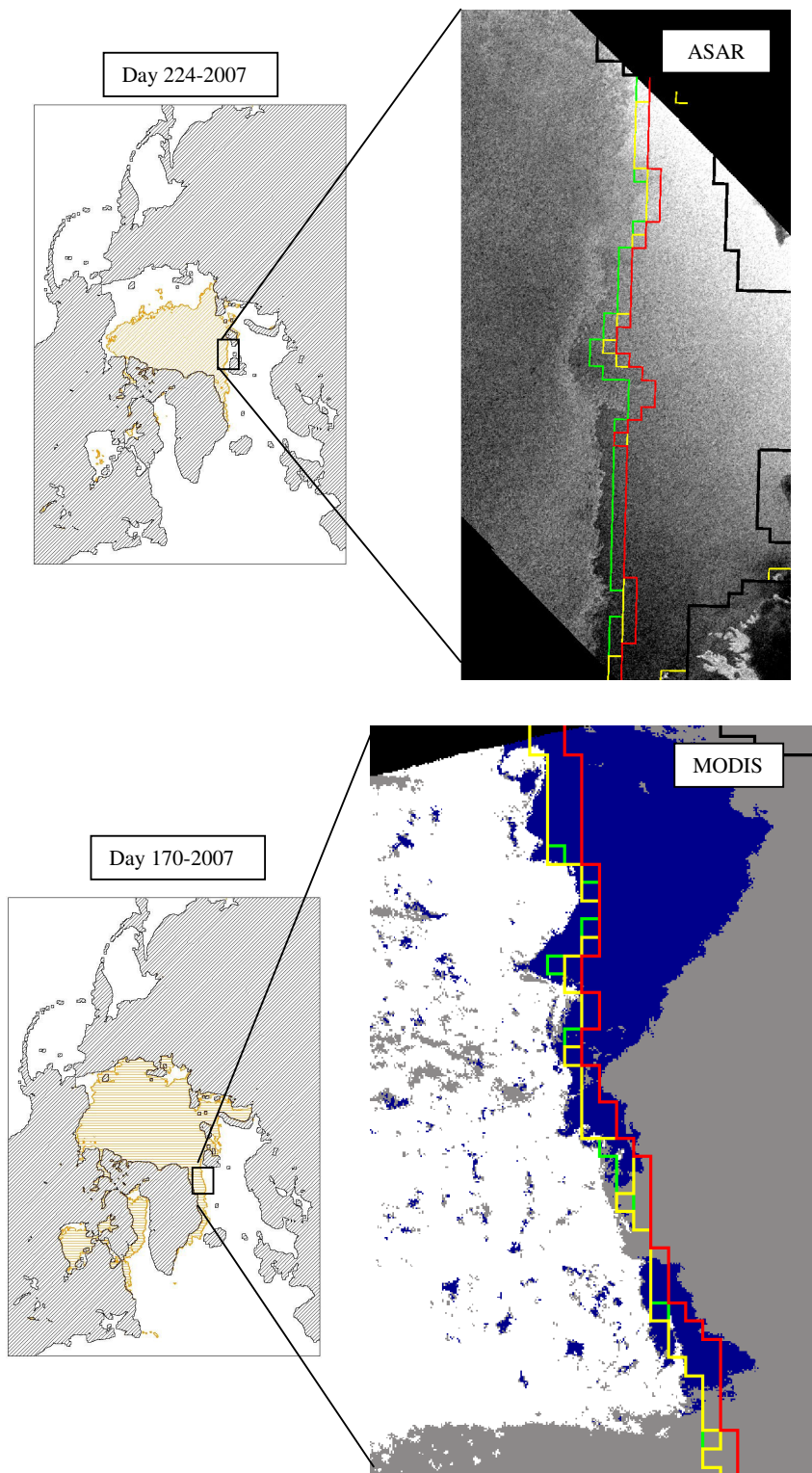


Figure 18 – Satellite microwave sea ice extents against MODIS and ASAR imagery
 [Green is AMSR (NT2), yellow is QSCAT (BYU SIRF) and red is QSCAT (KNMI 1.5 dB)]
 In MODIS image, grey represents possibly cloudy areas.

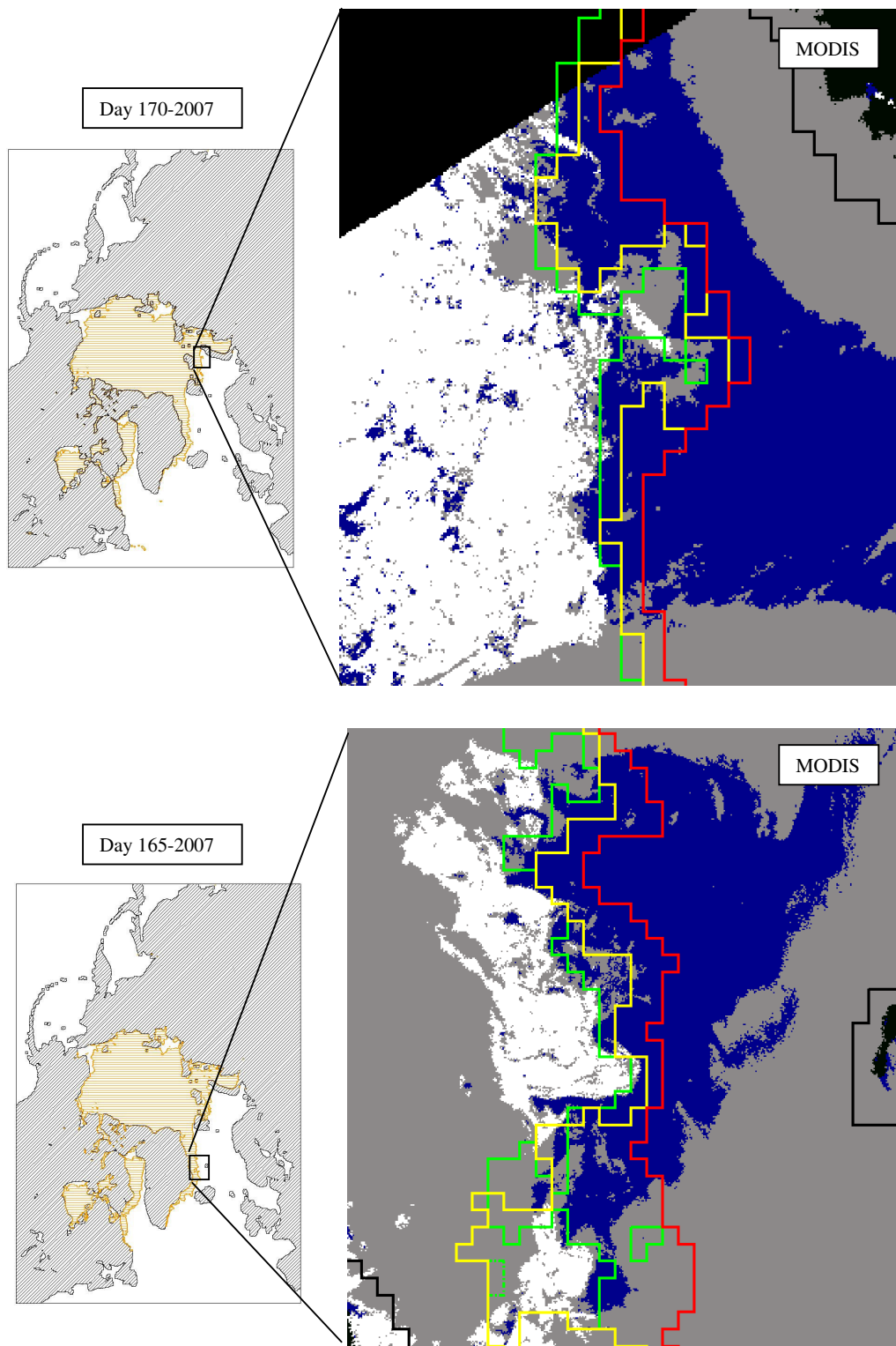


Figure 19 – Satellite microwave sea ice extents against MODIS and ASAR imagery
 [Green is AMSR (NT2), yellow is QSCAT (BYU SIRF) and red is QSCAT (KNMI 1.5 dB)]
 In MODIS image, grey represents possibly cloudy areas.

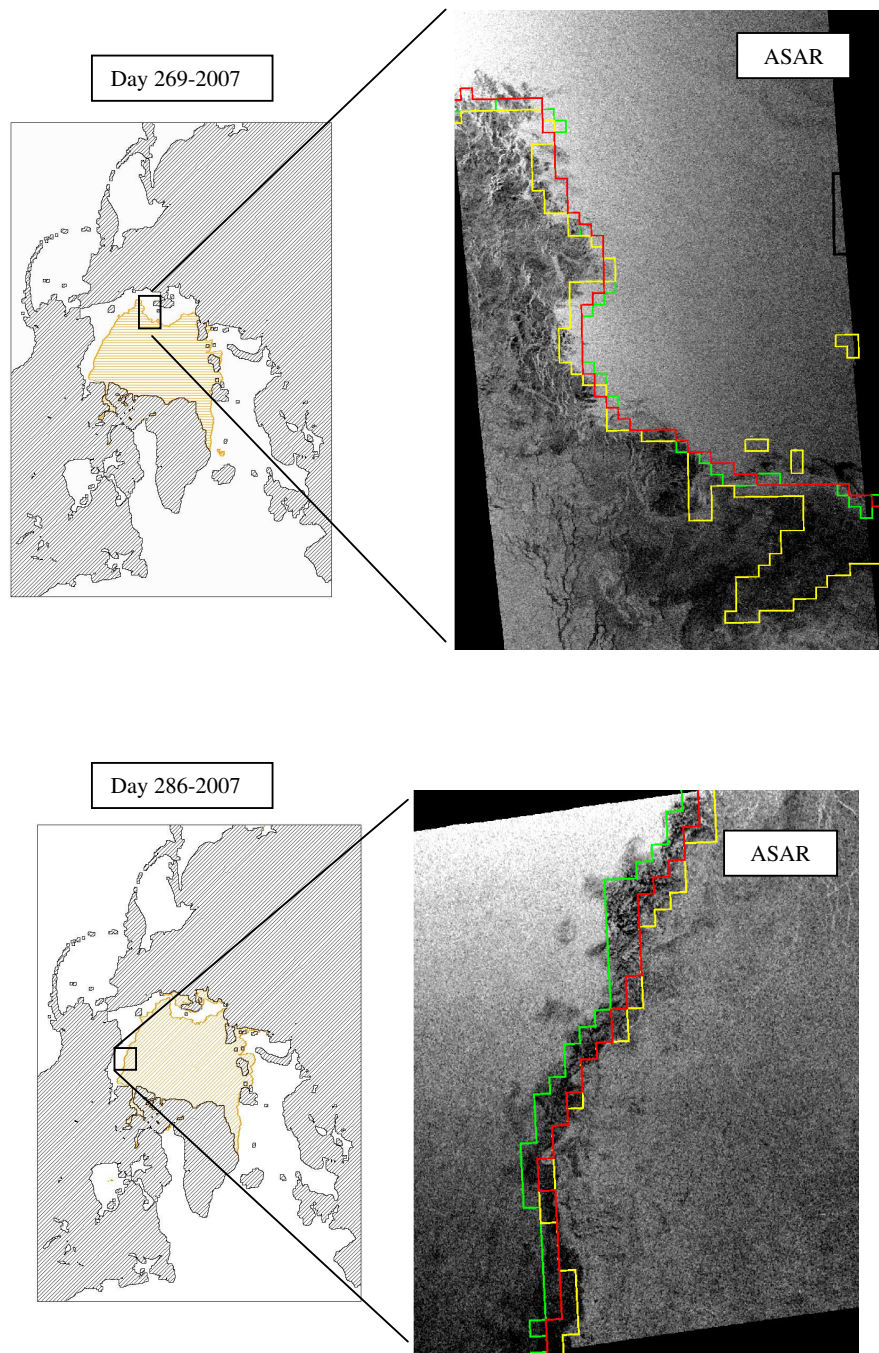


Figure 20 – Satellite microwave sea ice extents against MODIS and ASAR imagery
 [Green is AMSR (NT2), yellow is QSCAT (BYU SIRF) and red is QSCAT (KNMI 1.5 dB)]

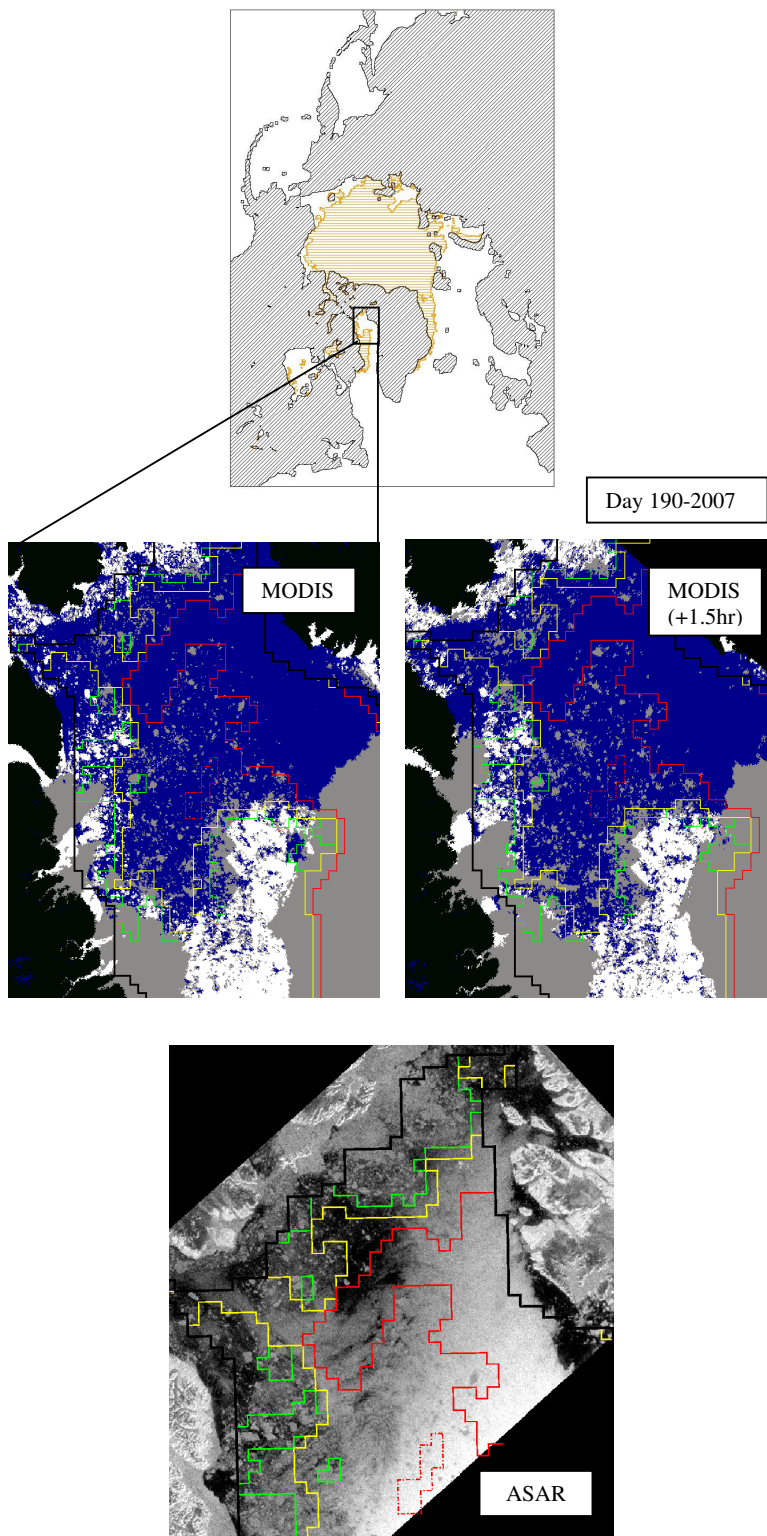


Figure 21 – Satellite microwave sea ice extents against MODIS and ASAR imagery
 [Green is AMSR (NT2), yellow is QSCAT (BYU SIRF) and red is QSCAT (KNMI 1.5 dB)]
 In MODIS image, grey represents possibly cloudy areas.

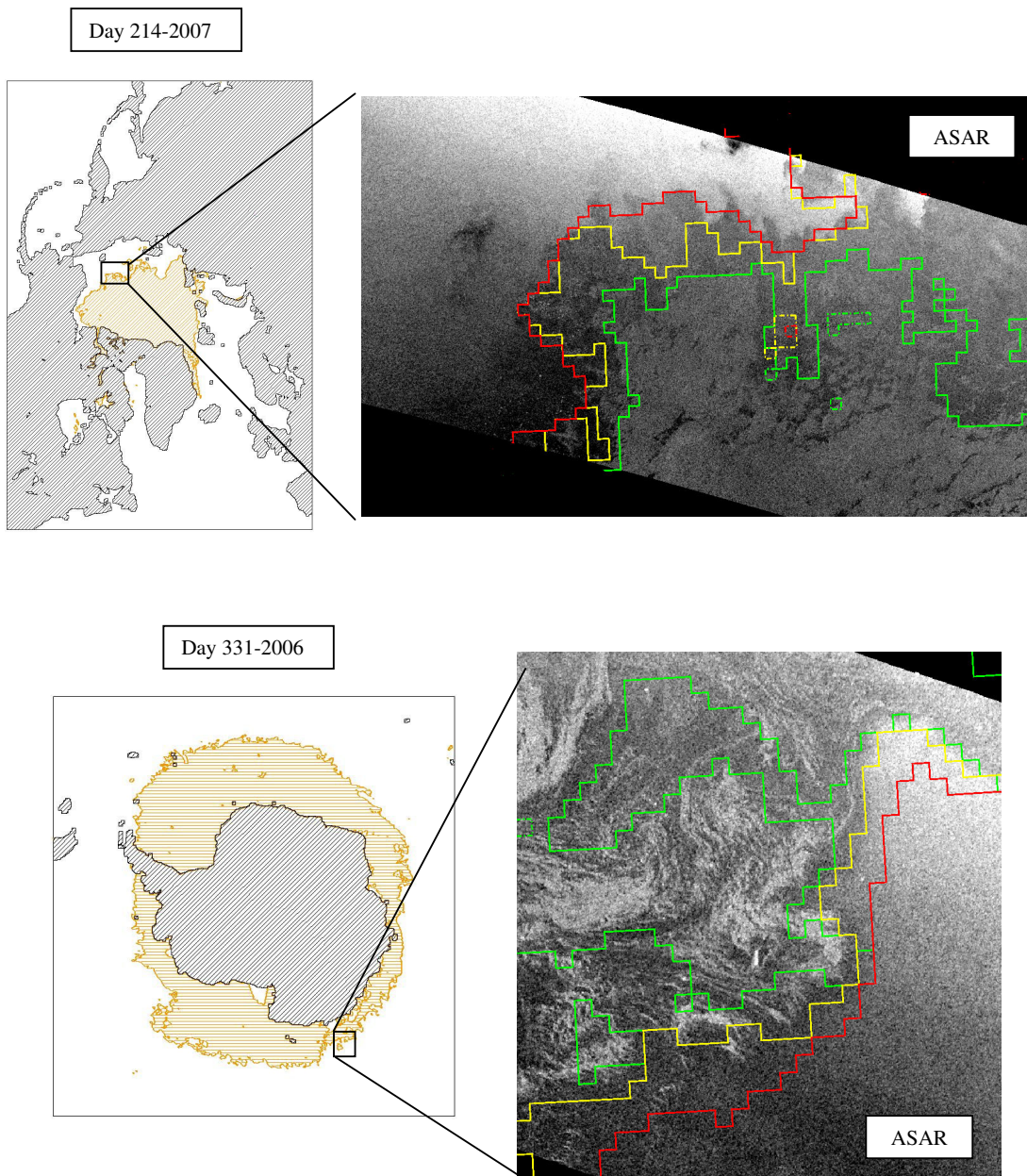


Figure 22 – Satellite microwave sea ice extents against MODIS and ASAR imagery
 [Green is AMSR (NT2), yellow is QSCAT (BYU SIRF) and red is QSCAT (KNMI 1.5 dB)]

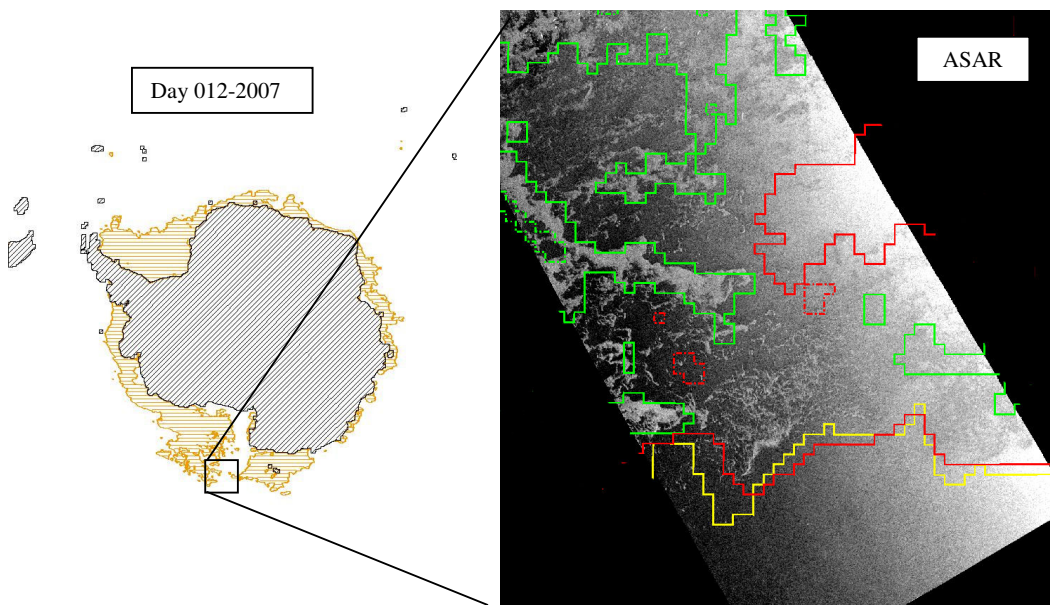
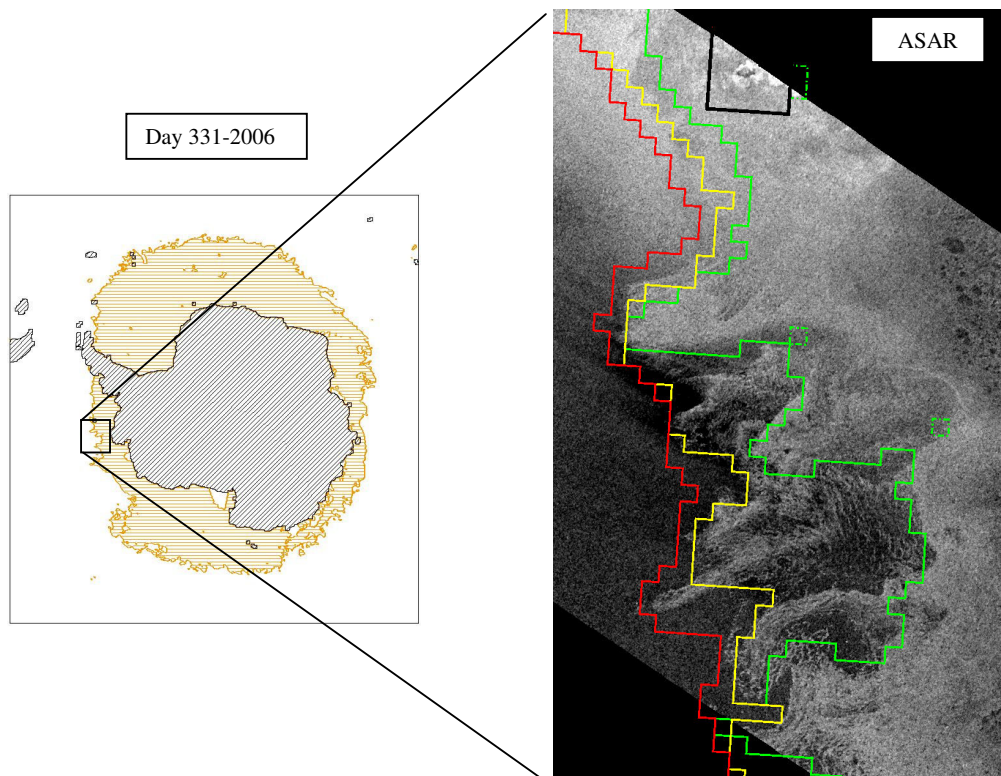


Figure 22 – Satellite microwave sea ice extents against MODIS and ASAR imagery
 [Green is AMSR (NT2), yellow is QSCAT (BYU SIRF) and red is QSCAT (KNMI 1.5 dB)]

5.3 Problems and fixes

After thorough testing and validation of the KNMI SeaWinds Bayesian algorithm for sea ice discrimination, there remain two issues adversely affecting its overall performance. To note:

- i) *Intersecting ocean wind and sea ice GMFs*: The discrimination power of the KNMI Bayesian algorithm is adversely affected in those regions where the empirical model functions for ocean wind and sea ice backscatter intersect in the measurement space. For the SeaWinds observation geometry, the region of ice/ocean GMF overlap corresponds with the high wind speed tail of the ocean wind GMF, which coincides with the bright multiyear ice (or ice sheet) tail of the sea ice GMF.

To correct for this problem, we introduce an additional piece of information, namely the location of the point of minimum distance on the ocean GMF (i.e. the retrieved wind) relative to the NWP wind forecast. It can be seen that the minimum distance *to* the GMF and the location of the point of minimum distance *on* the GMF are independent pieces of information. Using Bayes rule, the probability of a surface cell being ice given both backscatter measurements and NWP wind forecasts will be calculated as:

$$p(\text{ice} | \sigma^0, \bar{v}) = \frac{p(\sigma^0, \bar{v} | \text{ice})p(\text{ice})}{p(\sigma^0, \bar{v} | \text{ice})p(\text{ice}) + p(\sigma^0, \bar{v} | \text{ocean})p(\text{ocean})}$$

Where:

$$p(\sigma^0, \bar{v} | \text{ice}) = p(\sigma^0 | \text{ice})p(\bar{v} | \text{ice})$$

$$p(\sigma^0, \bar{v} | \text{ocean}) = p(\sigma^0 | \text{ocean})p(\bar{v} | \text{ocean})$$

Arriving at:

$$p(\text{ice} | \sigma^0, \bar{v}) = \frac{p(\sigma^0 | \text{ice})p(\bar{v} | \text{ice})p(\text{ice})}{p(\sigma^0 | \text{ice})p(\bar{v} | \text{ice})p(\text{ice}) + p(\sigma^0 | \text{ocean})p(\bar{v} | \text{ocean})p(\text{ocean})}$$

Where $p(\sigma^0 | \text{ocean})$ and $p(\sigma^0 | \text{ice})$ are the already known distributions of ocean and ice backscatter measurements about the “wind cone” and the “ice line” models, while $p(\bar{v} | \text{ocean})$ and $p(\bar{v} | \text{ice})$ refer to the distribution of wind retrievals over ocean and ice surfaces respectively, modelled as:

$$p(\bar{v} | \text{ocean}) = \text{Normal distribution about NWP wind} = 1/(2\pi\Delta^2) \exp[-|\bar{v} - \bar{v}_{NWP}|^2 / (2\Delta^2)]$$

$$p(\bar{v} | \text{ice}) = \text{Uniform distribution} = 1/(2\pi\Delta^2)$$

The standard deviation of retrieved wind solutions about NWP wind forecasts has been set to $\Delta = 10$ m/s. This approach solves the problem with intersecting GMF functions effectively and also proves beneficial for the detection of low concentration and thin ice in the marginal ice zones.

- ii) *Ocean noise (rain signature)*: There is a penalty to increasing the tolerance in sea ice detection with scatterometer algorithms, which consists in enhanced ocean noise (i.e. ocean that is misclassified as ice). This ocean noise arises typically from rain contaminated cells because rain and ice both share a similar backscatter signature. Most of this ocean noise can be filtered using a brightness temperature based threshold [Ezraty, 2000] or a SST based mask for those areas far from the ice edge.

Thin ice, low concentration ice and rain contaminated cells all share a similar backscatter signature which is characteristic of a mixed surface/volume interaction. Figure 23 shows the effects of rain on measured ocean backscatter and the distribution of rain contaminated observations in the measurement space of SeaWinds backscatter data. The upper panel shows that the rain signature dominates the backscatter measurement at low windspeeds. The lower panel shows that rain saturated measurements lie in the vicinity of the ice model, making it difficult to separate them in terms of backscatter alone.

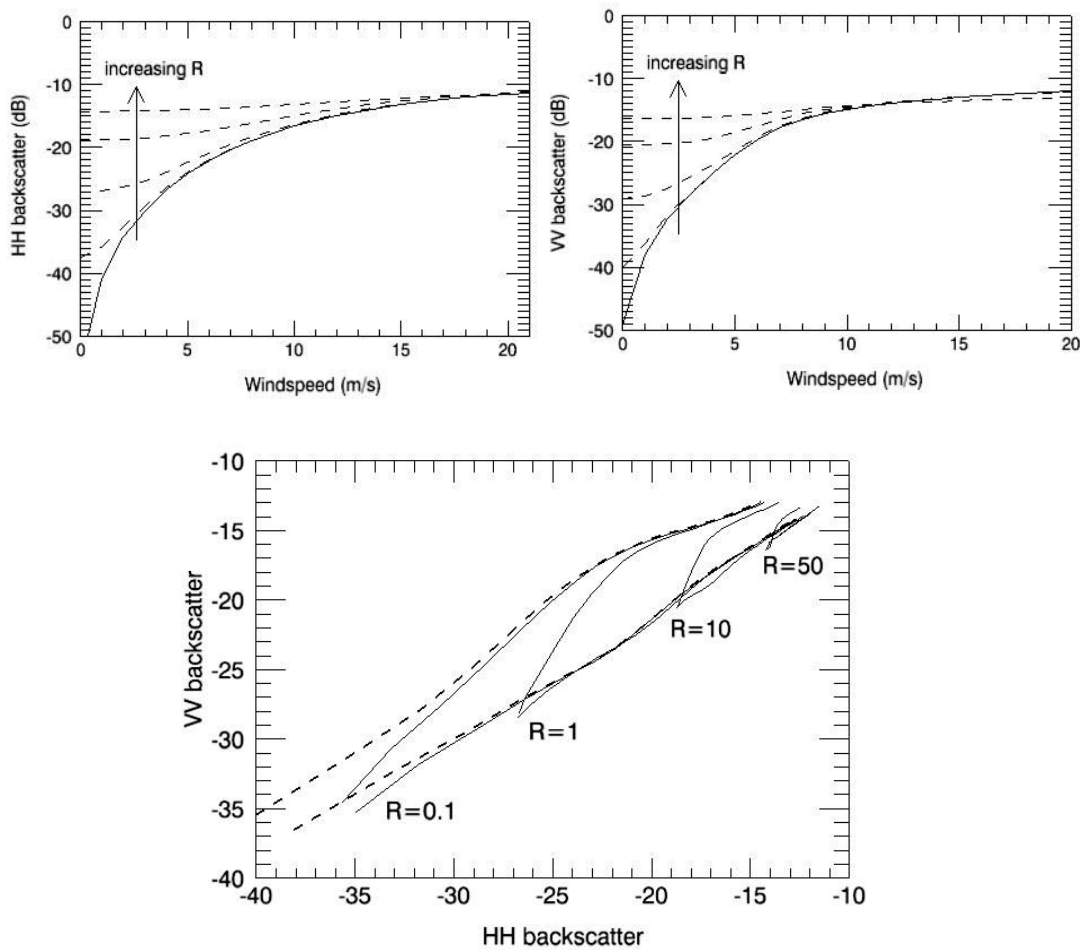


Figure 23 – Rain effects on distribution of backscatter in QSCAT measurement space (R is columnar rain rate in $\text{km}\cdot\text{mm}/\text{hr}$, from [Draper, 2004])

Figure 24 below shows the distribution of SeaWinds brightness temperatures for ocean, sea ice and rain flagged cells. These figures illustrate the fact that rain cells are definitely warmer than sea ice, rendering these two species effectively separable in terms of their brightness temperatures.

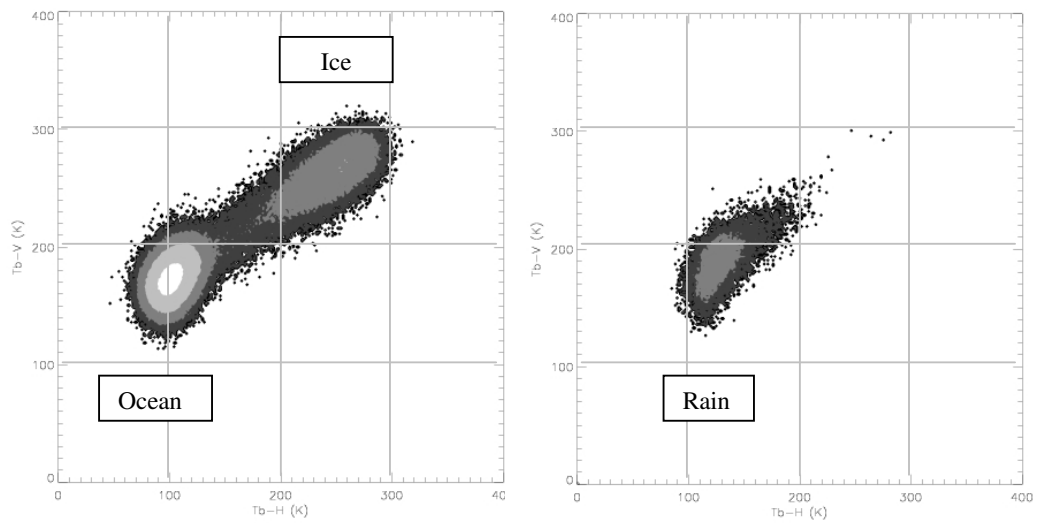
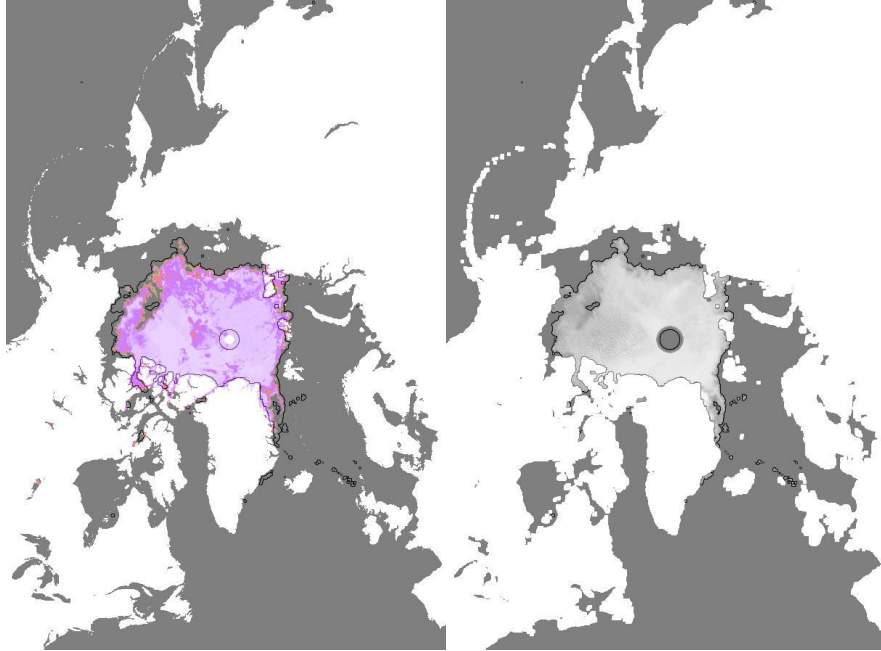


Figure 24 – Sample distributions of ice/ocean (left) and rain (right) brightness temperatures



Sep 15th 2006

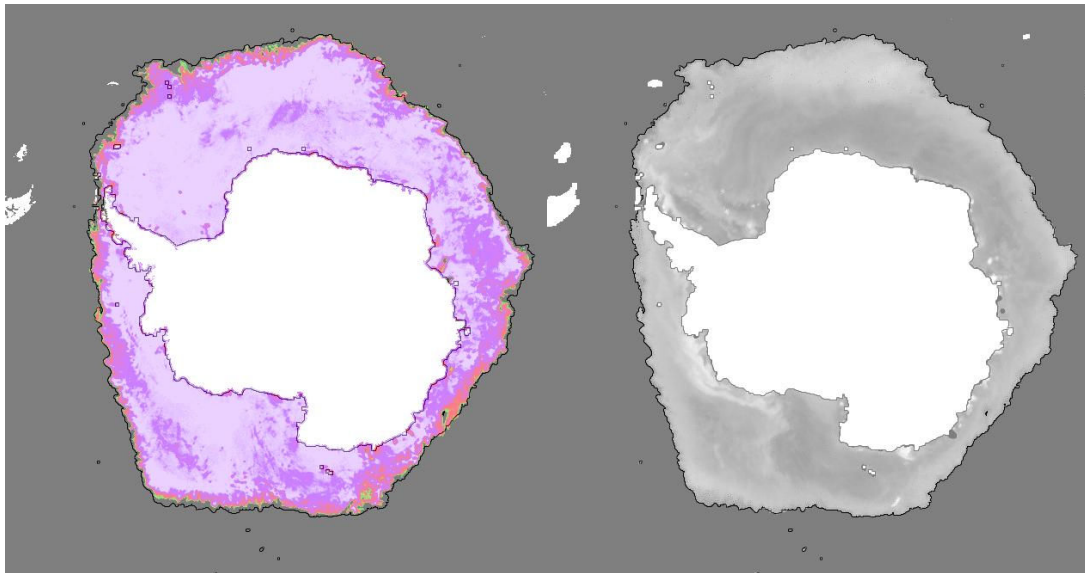
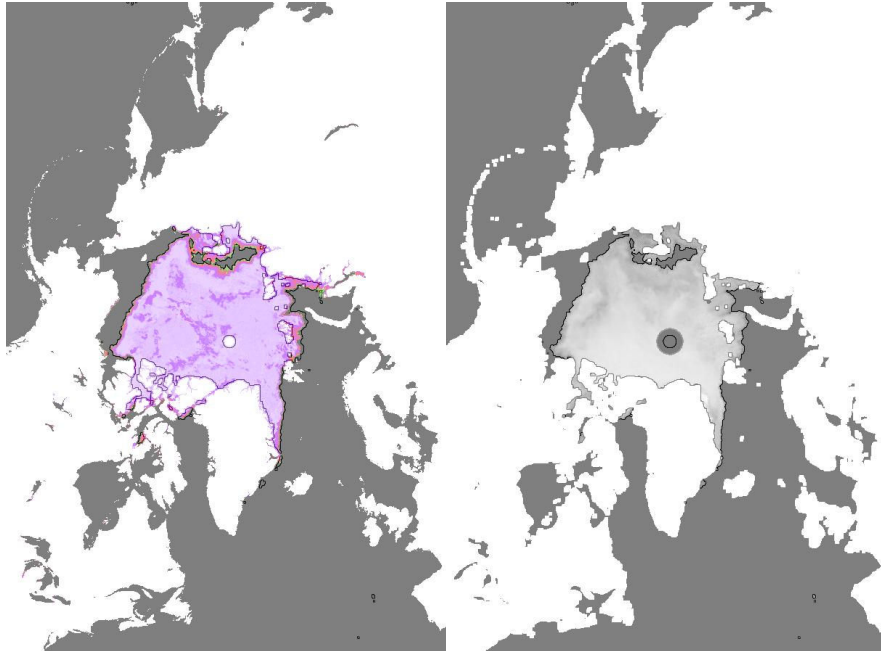


Figure 25 – QSCAT KNMI (1.5 dB) ice edge vs AMSR sea ice concentration (LEFT) and QSCAT ice brightness (RIGHT)



Oct 15th 2006

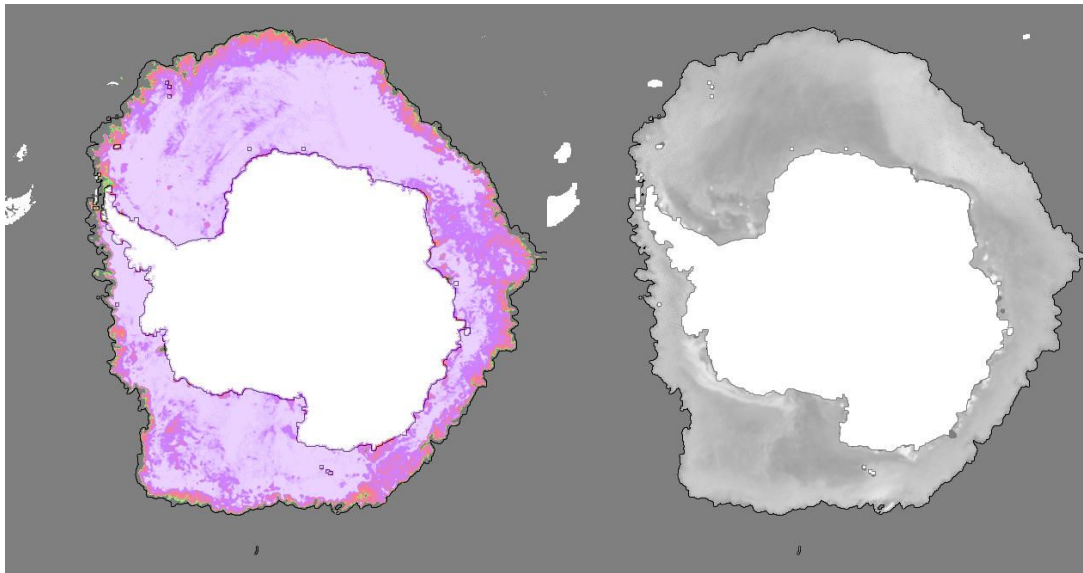
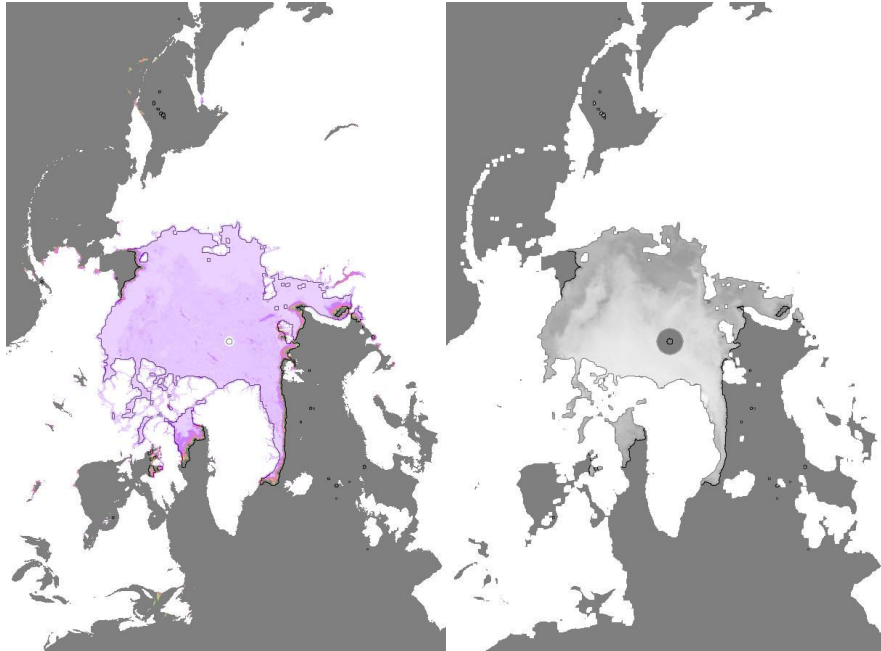


Figure 26 – QSCAT KNMI (1.5 dB) ice edge vs AMSR sea ice concentration (LEFT) and QSCAT ice brightness (RIGHT)



Nov 15th 2006

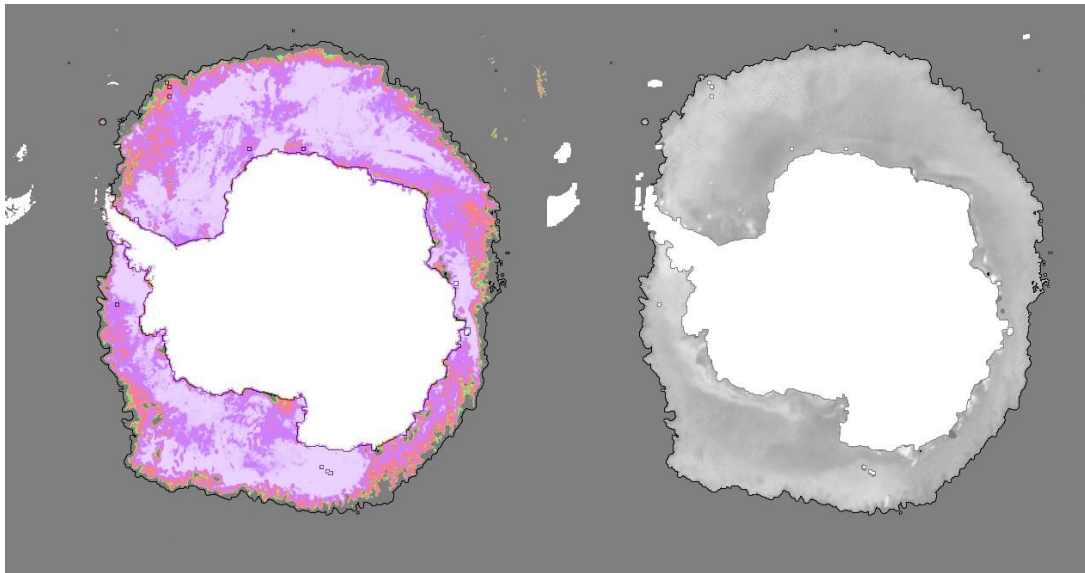
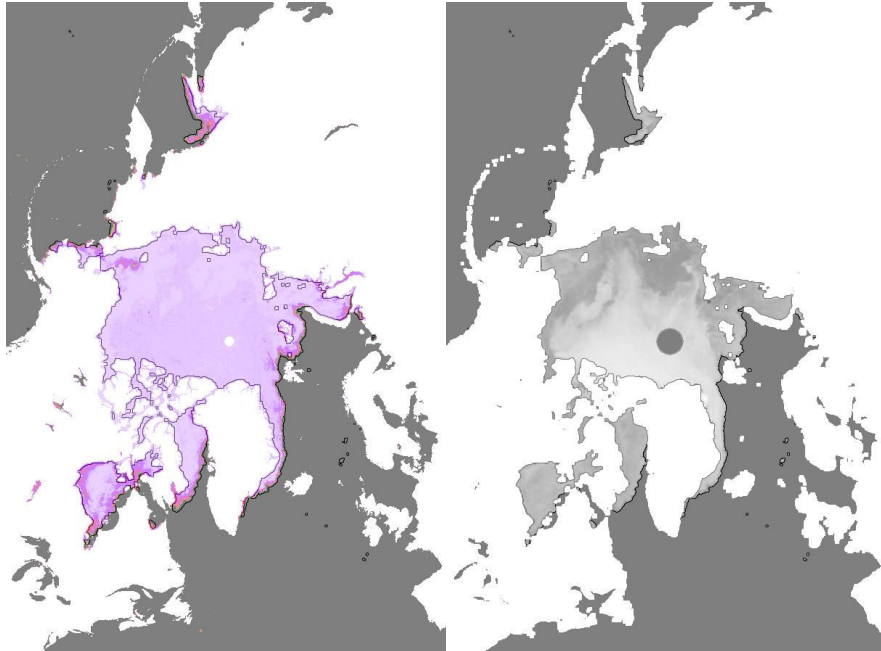


Figure 27 – QSCAT KNMI (1.5 dB) ice edge vs AMSR sea ice concentration (LEFT) and QSCAT ice brightness (RIGHT)



Dec 15th 2006

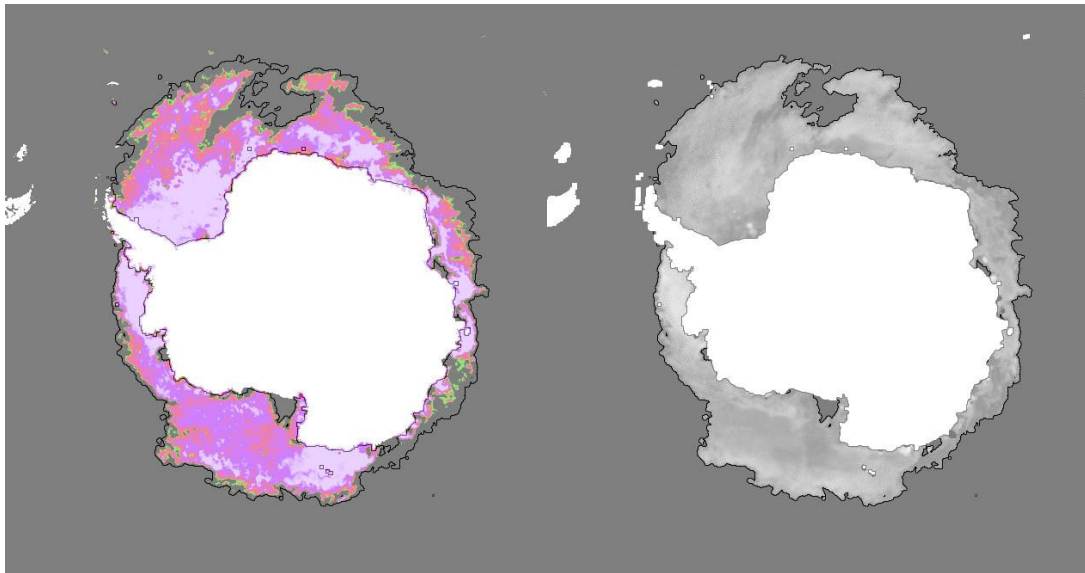
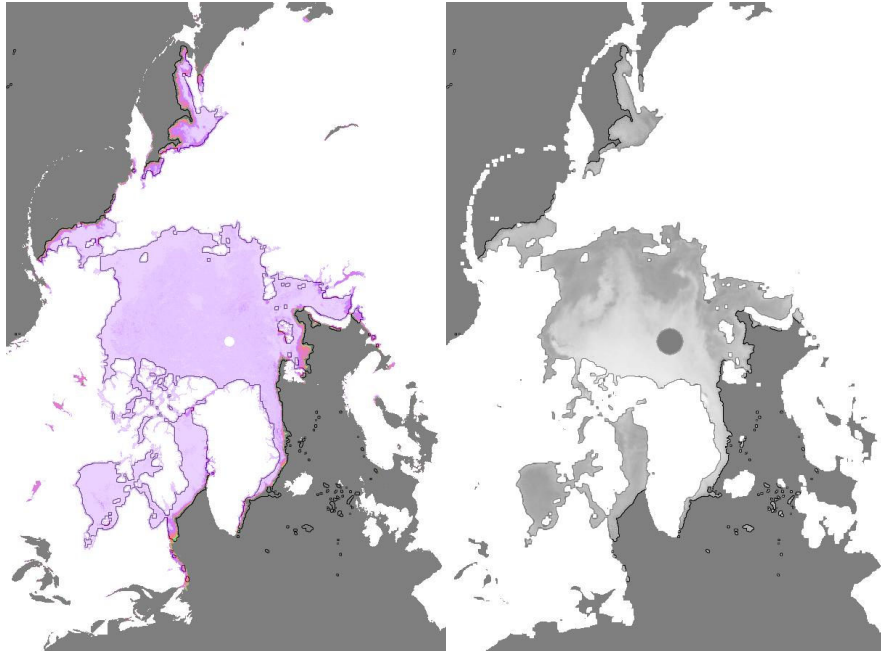


Figure 28 – QSCAT KNMI (1.5 dB) ice edge vs AMSR sea ice concentration (LEFT) and QSCAT ice brightness (RIGHT)



Jan 15th 2007

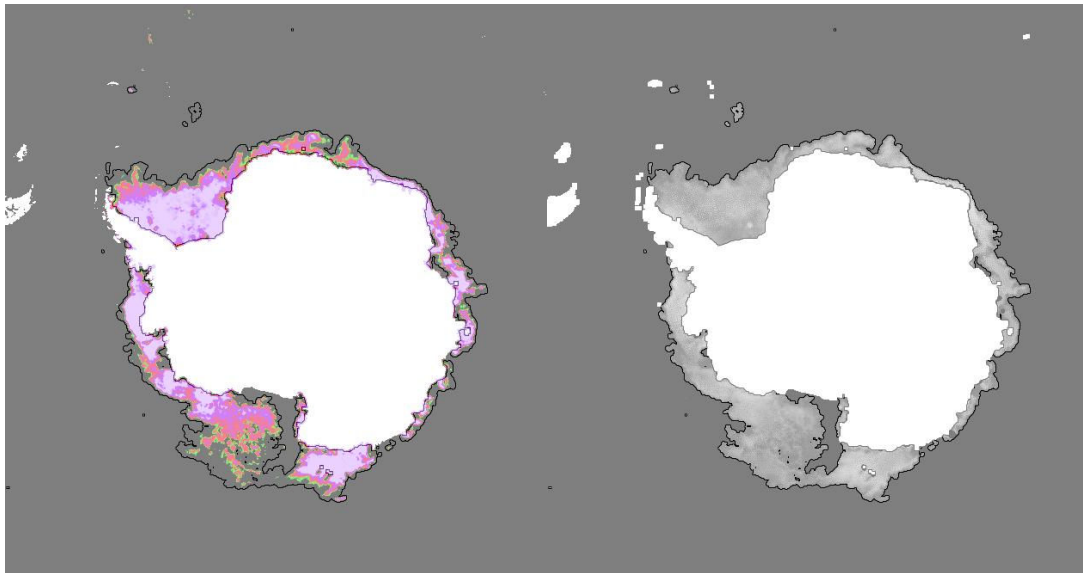
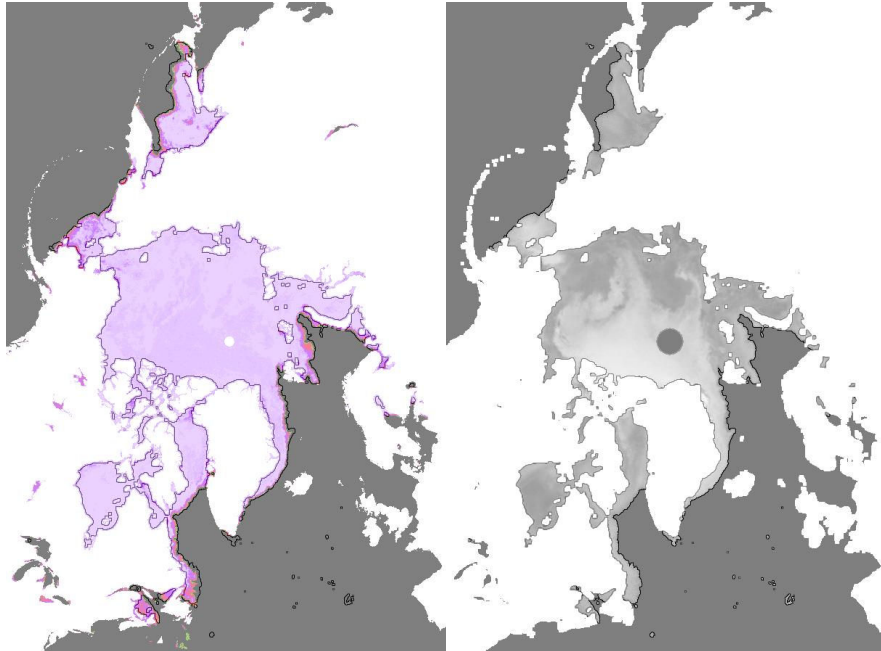


Figure 29 – QSCAT KNMI (1.5 dB) ice edge vs AMSR sea ice concentration (LEFT) and QSCAT ice brightness (RIGHT)



Feb 15th 2007

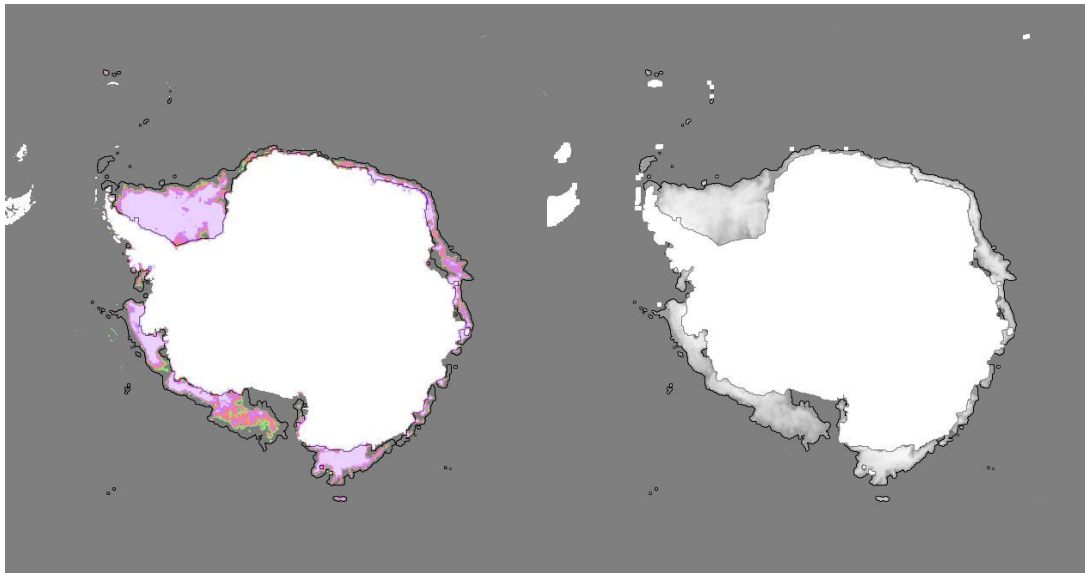
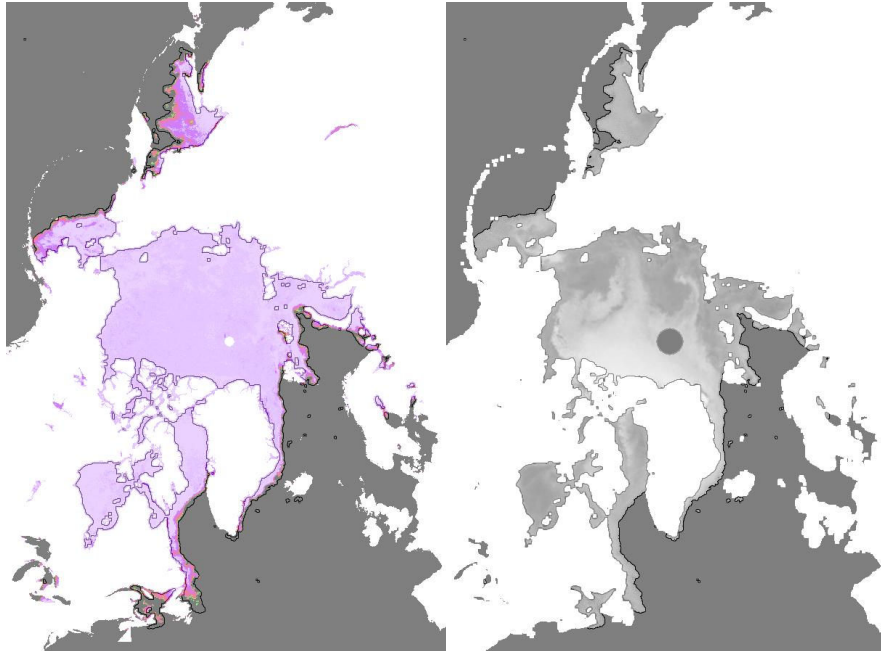


Figure 30 – QSCAT KNMI (1.5 dB) ice edge vs AMSR sea ice concentration (LEFT) and QSCAT ice brightness (RIGHT)



Mar 15th 2007

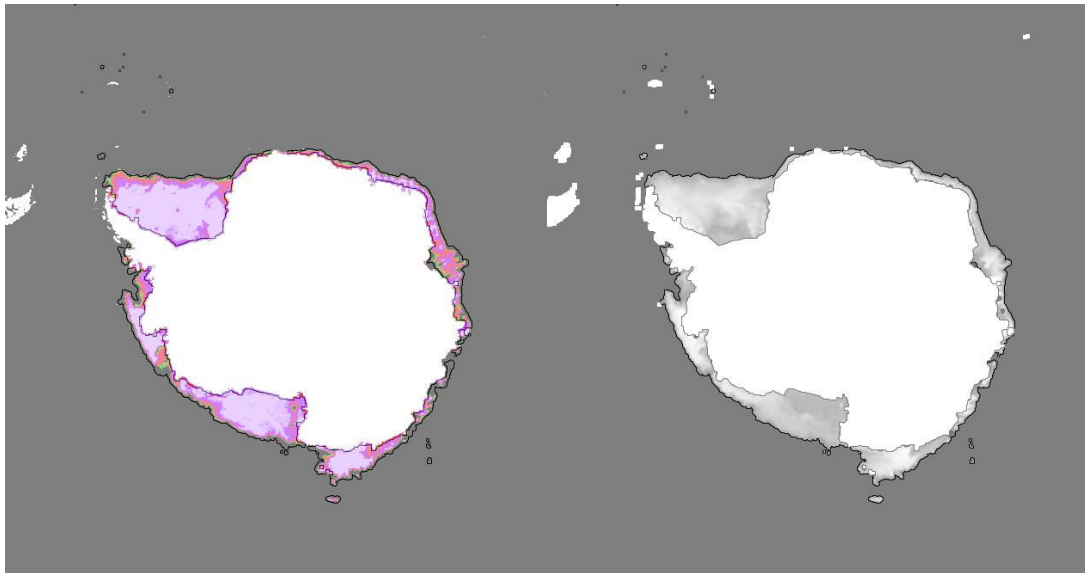
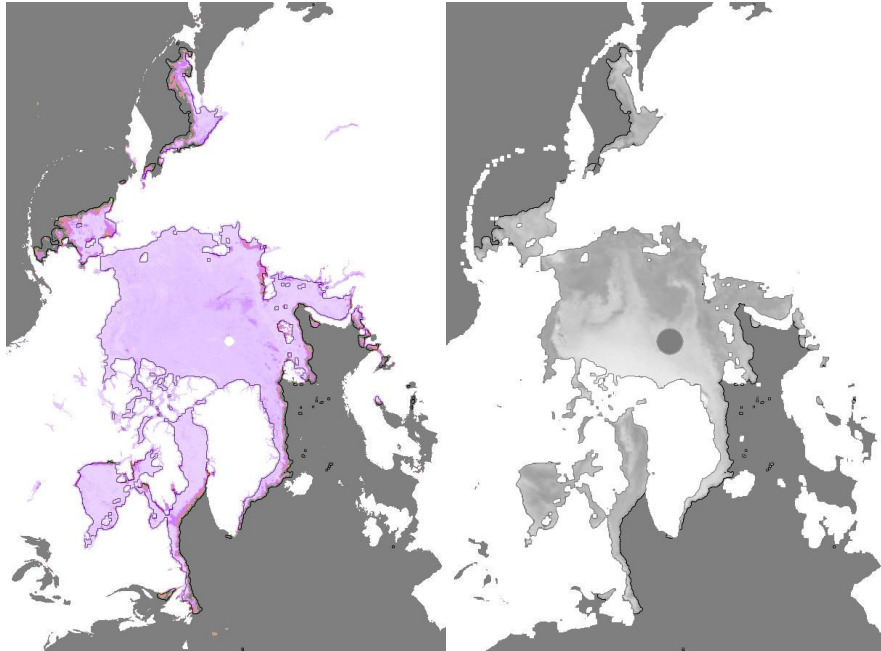


Figure 31 – QSCAT KNMI (1.5 dB) ice edge vs AMSR sea ice concentration (LEFT) and QSCAT ice brightness (RIGHT)



Apr 15th 2007

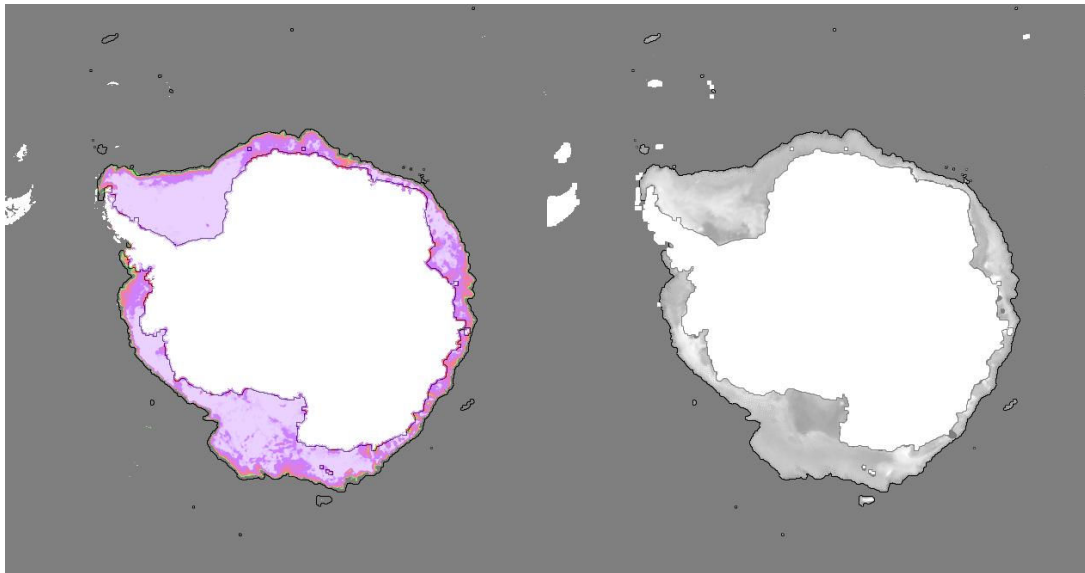
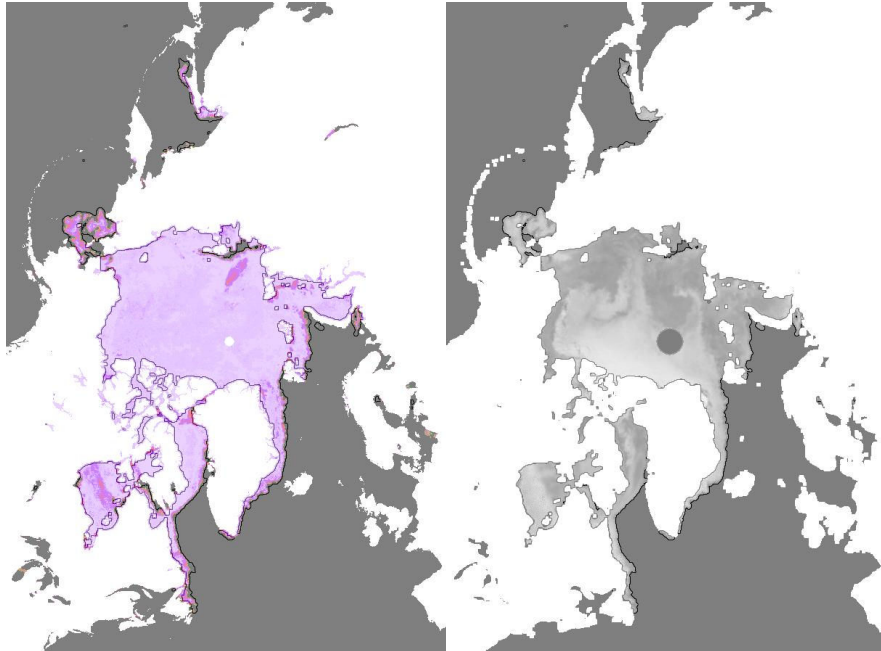


Figure 32 – QSCAT KNMI (1.5 dB) ice edge vs AMSR sea ice concentration (LEFT) and QSCAT ice brightness (RIGHT)



May 15th 2007

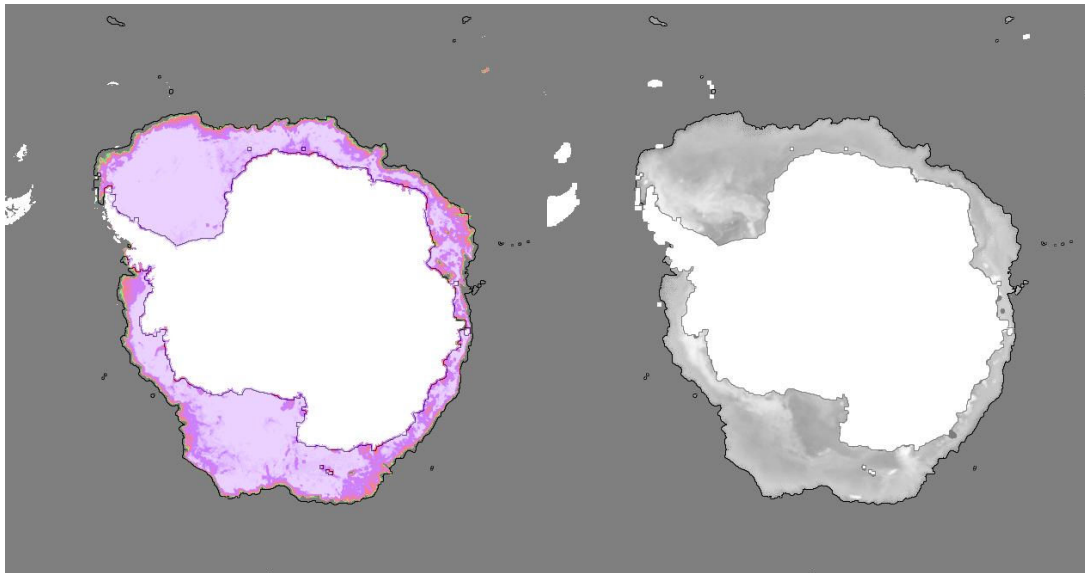
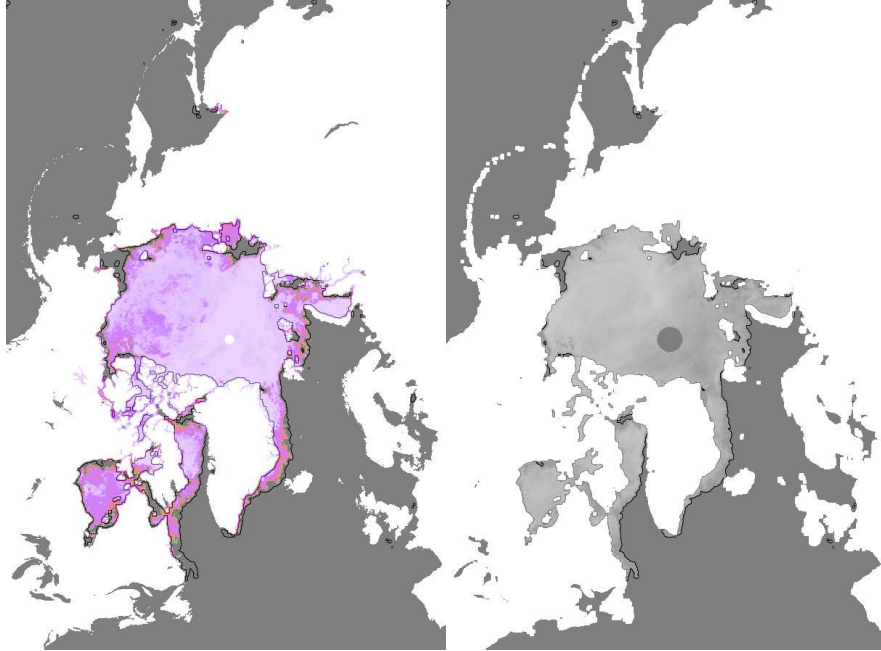


Figure 33 – QSCAT KNMI (1.5 dB) ice edge vs AMSR sea ice concentration (LEFT) and QSCAT ice brightness (RIGHT)



Jun 15th 2007

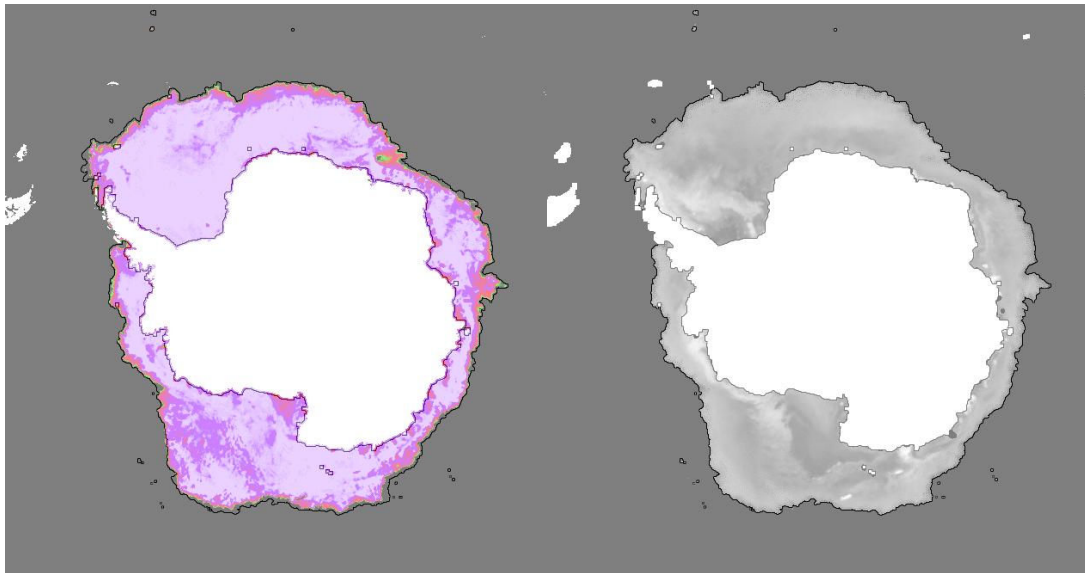
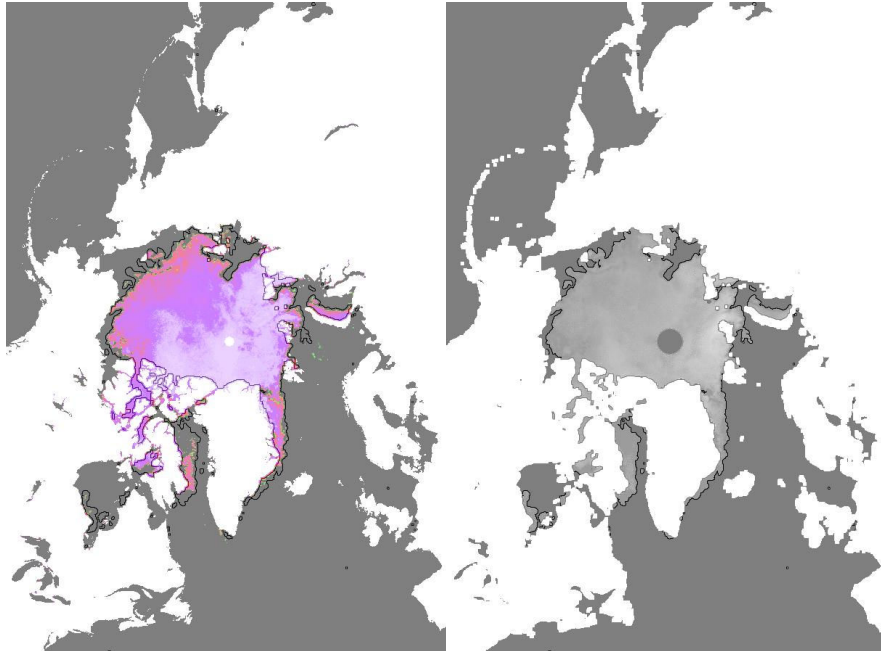


Figure 34 – QSCAT KNMI (1.5 dB) ice edge vs AMSR sea ice concentration (LEFT) and QSCAT ice brightness (RIGHT)



Jul 15th 2007

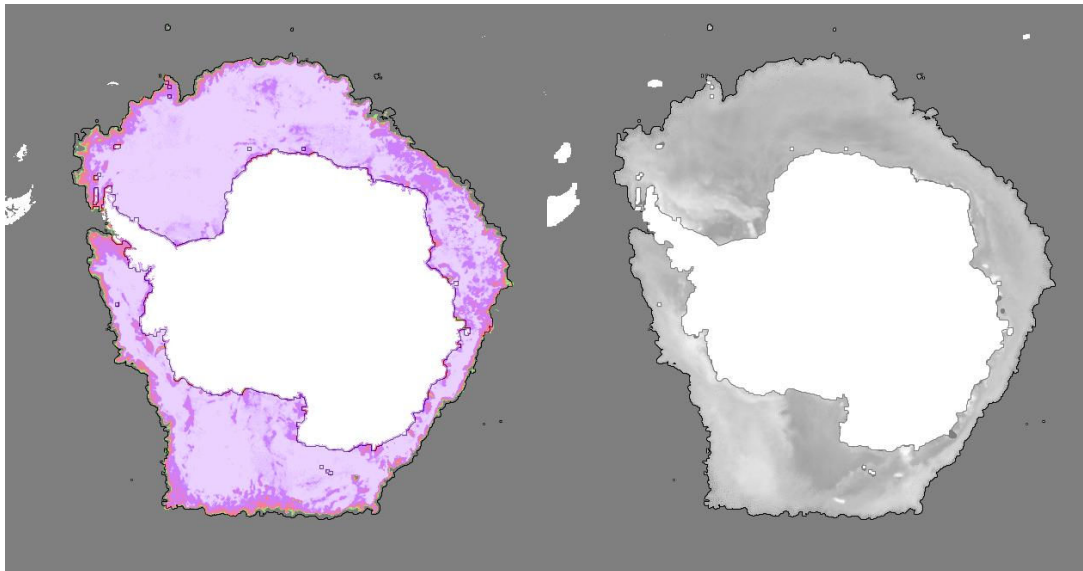
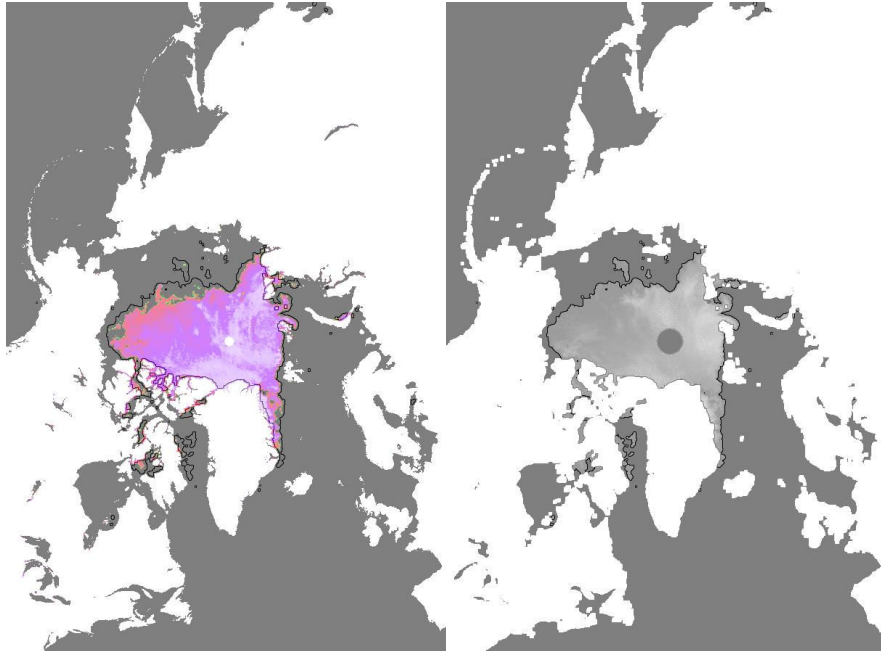


Figure 35 – QSCAT KNMI (1.5 dB) ice edge vs AMSR sea ice concentration (LEFT) and QSCAT ice brightness (RIGHT)



Aug 15th 2007

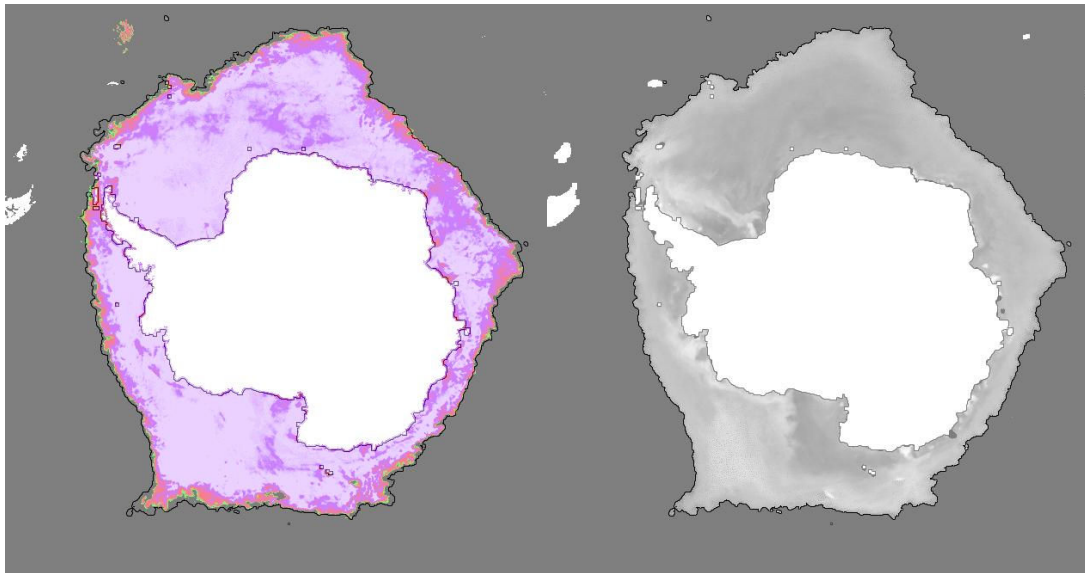
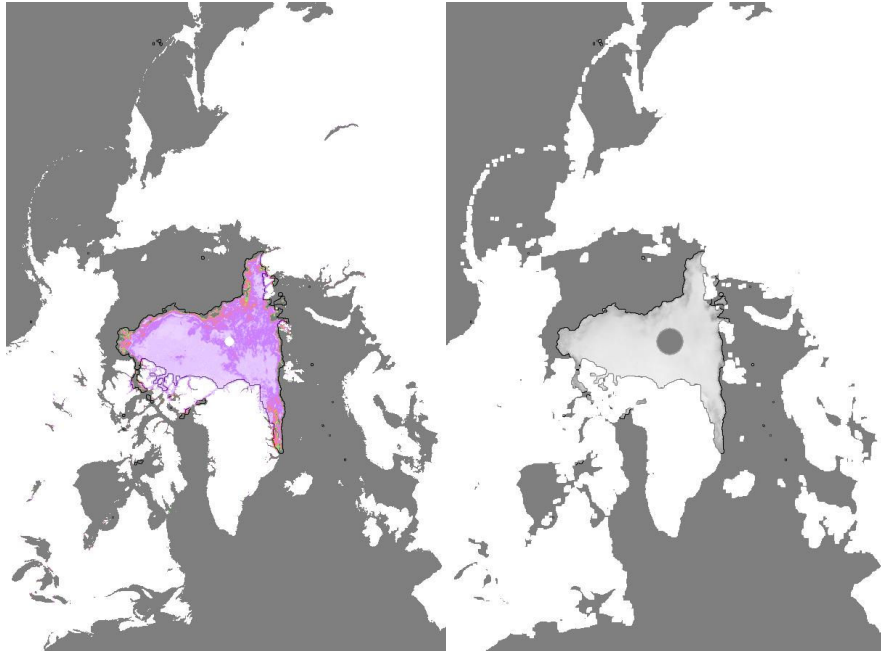


Figure 36 – QSCAT KNMI (1.5 dB) ice edge vs AMSR sea ice concentration (LEFT) and QSCAT ice brightness (RIGHT)



Sep 15th 2007

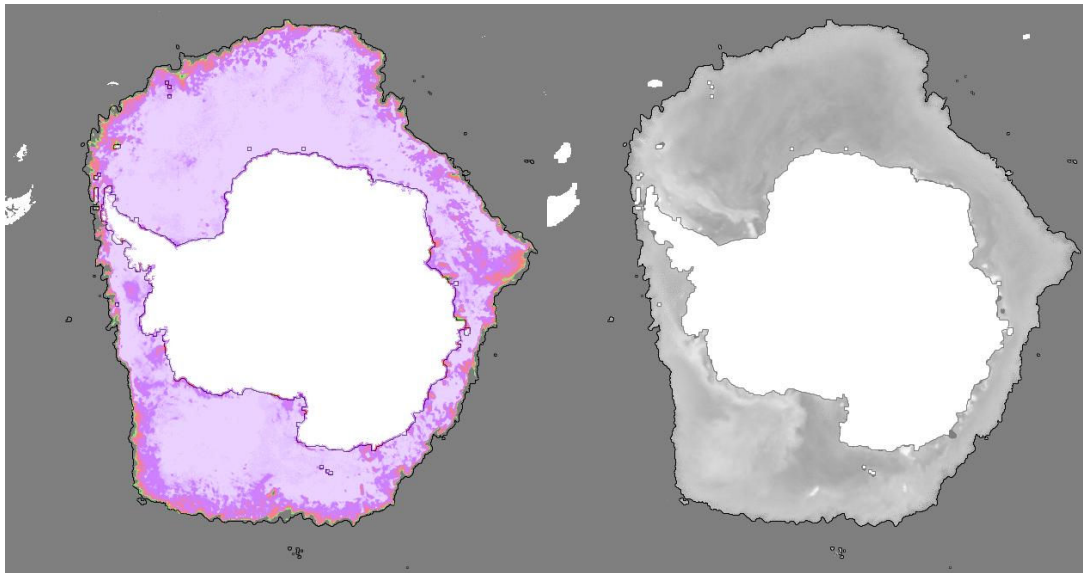


Figure 37 – QSCAT KNMI (1.5 dB) ice edge vs AMSR sea ice concentration (LEFT) and QSCAT ice brightness (RIGHT)

6 Summary and conclusions

In this report, we describe the implementation of a Near-Real Time sea ice detection algorithm using SeaWinds backscatter data. Well beyond the threshold-based contrasts between sea ice and ocean backscatter properties exploited in earlier algorithms, the KNMI Bayesian approach uses full geophysical model functions to discriminate sea ice from water returns. The fitted Ku-band ocean wind and sea ice models for SeaWinds, together with their measurement noise characteristics, are employed for sea ice detection. The normalized distances given by MLE residuals to the respective ocean and sea ice GMF manifolds are converted into sea ice and ocean wind conditional probabilities, and these are combined into a posterior probability using a Bayesian approach. The SeaWinds KNMI algorithm proves to be less noisy than the existing SeaWinds BYU algorithm and adjusts better to our primary validating reference (AMSR-NT2 sea ice concentrations) during the fall and winter months. The performance of the KNMI Bayesian algorithm during the spring and summer months has been validated using higher resolution MODIS and ASAR imagery, indicating substantial errors in AMSR NT2 sea ice extents during the melt season, which are related to the presence of lower concentration and water saturated sea ice in the marginal zones. The KNMI Bayesian algorithm provides a rather conservative definition of sea ice edge, more in line with that provided by ship observations and well-suited for applications that require reliable masking of sea ice all year round.

Aspects to be further elaborated include the determination of sea ice concentrations from conditional sea ice probabilities and the creation of a historic long-term record of QUIKSCAT sea ice extents from archived data.

Appendices

Appendix A

Empirical Ku-Band Ocean GMF (NSCAT2)

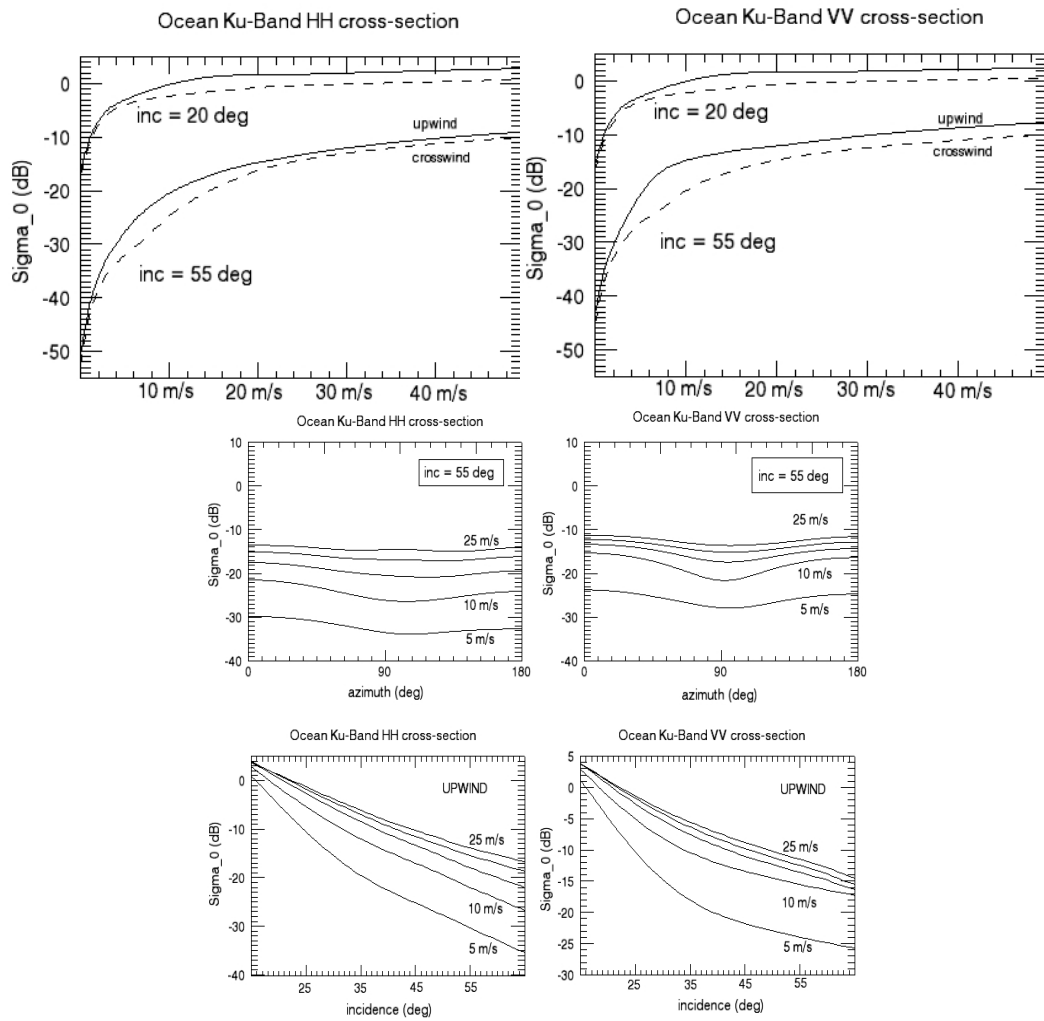
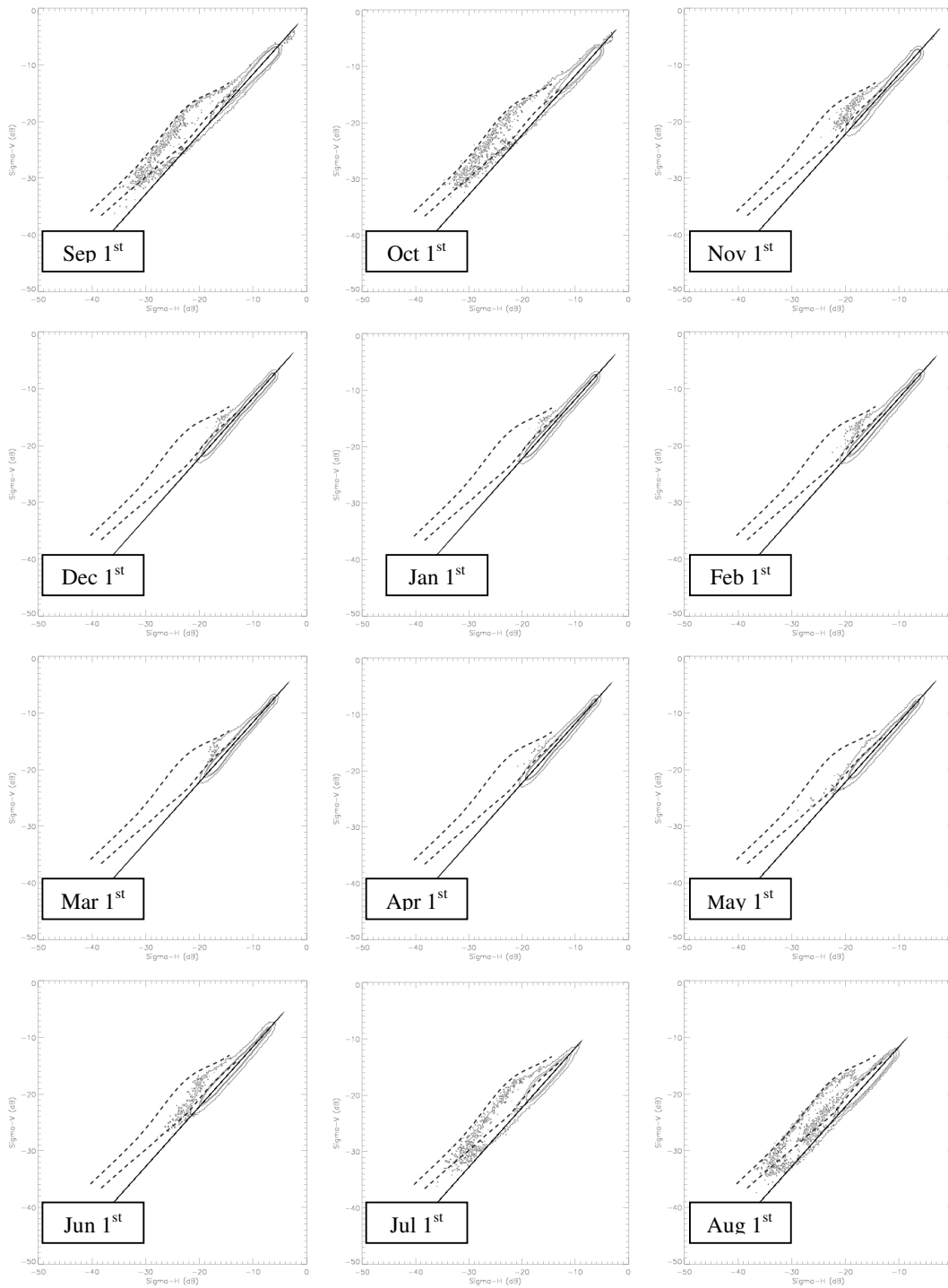


Figure A1 – Empirical Ku-Band GMF (a.k.a. NSCAT2)

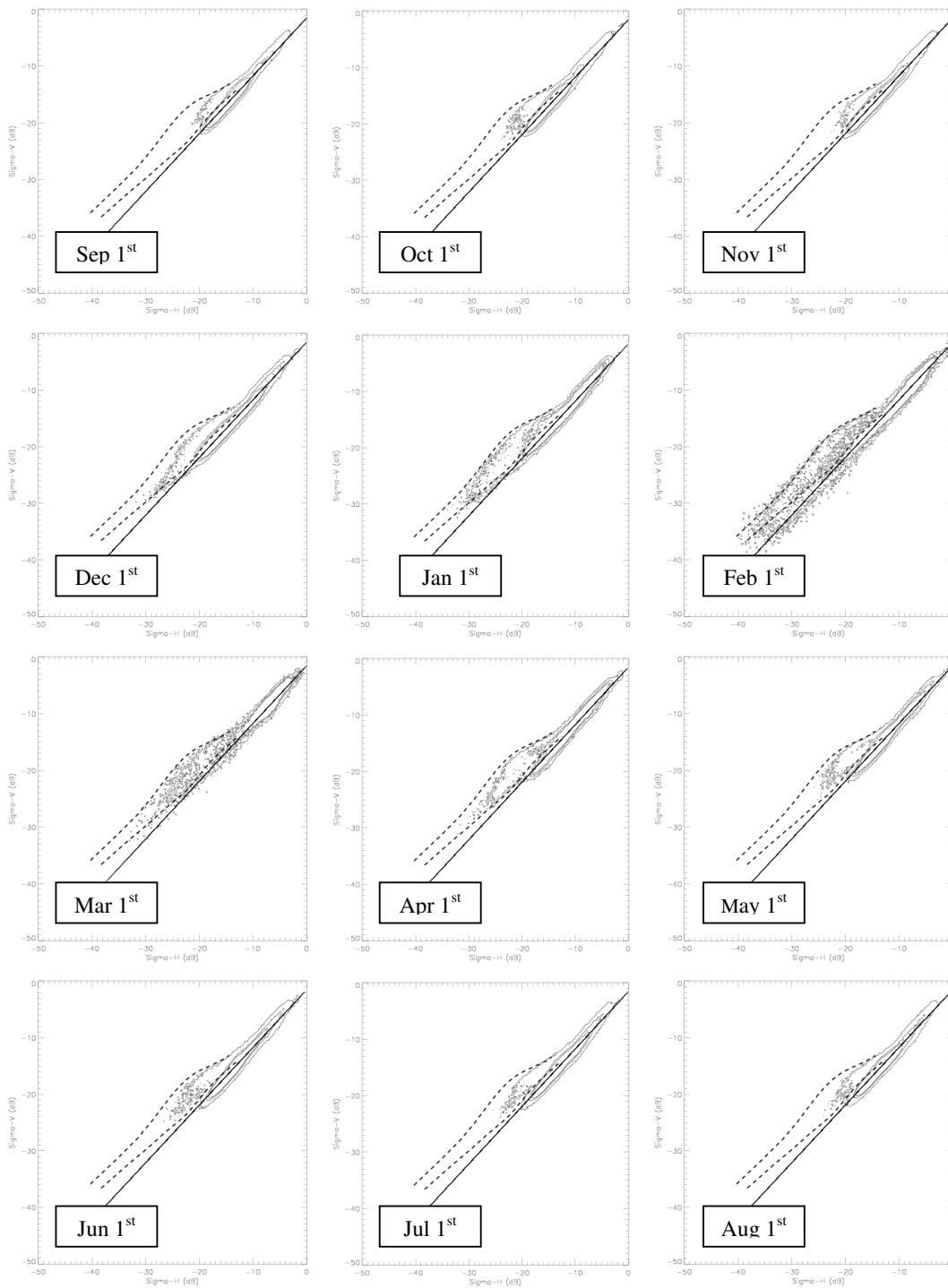
Appendix B1

Linear fits to sea ice backscatter (using BYU masks) Arctic



Appendix B2

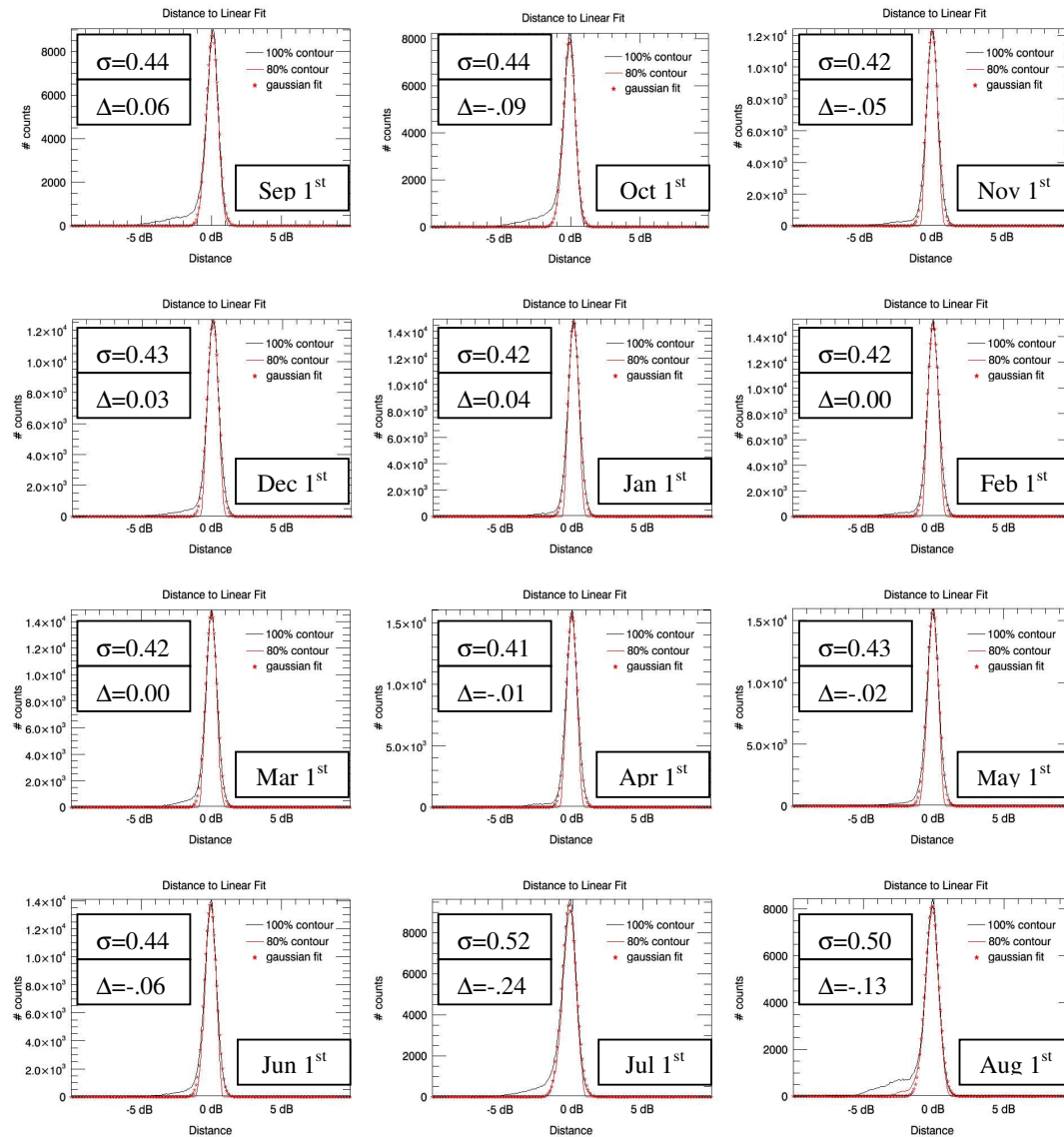
Linear fits to sea ice backscatter (BYU masks) Antarctic



Appendix C1

Scatter distribution – Distances to linear ice model (in dB space)

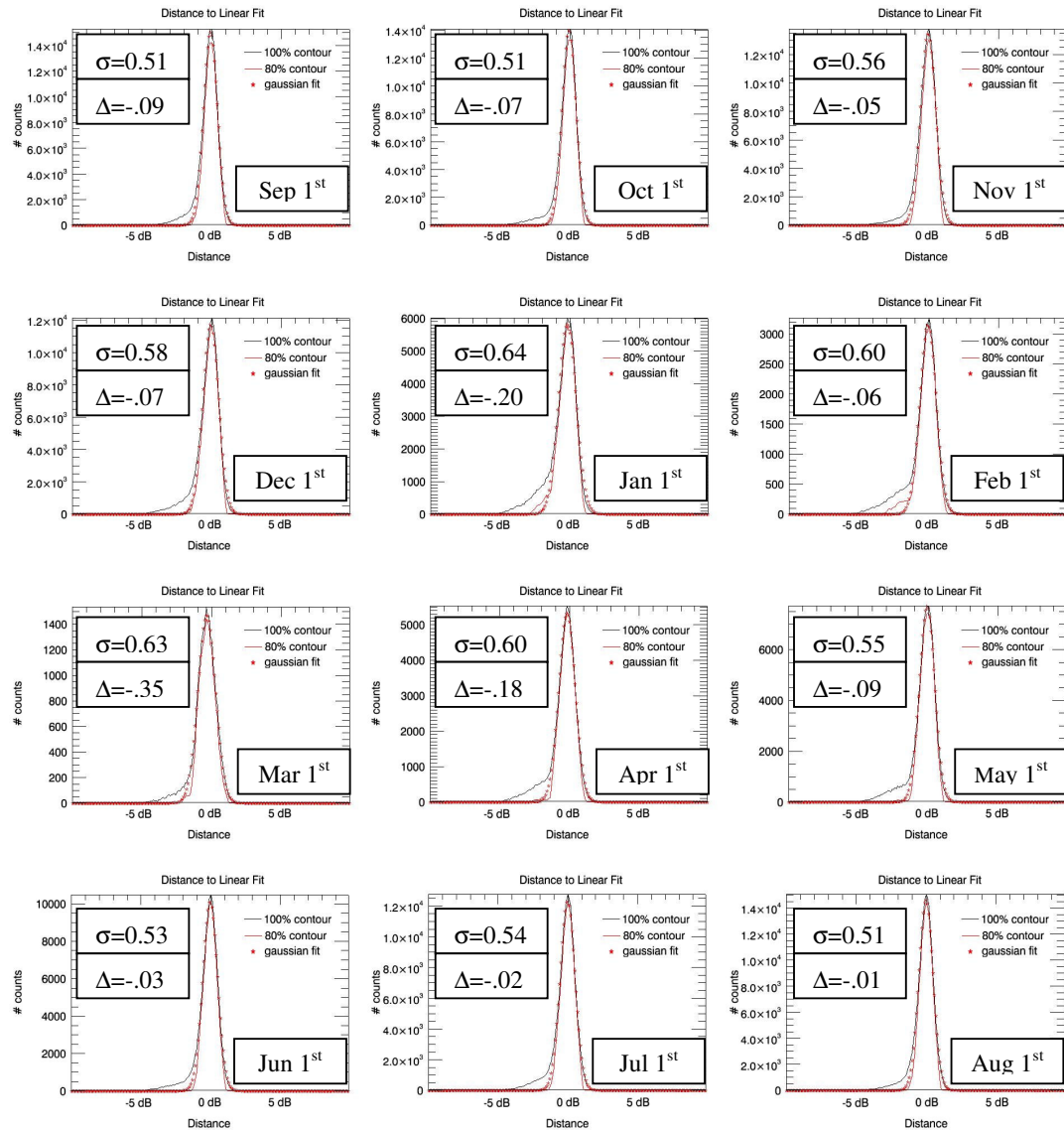
Arctic



Appendix C2

Scatter distribution – Distances to linear ice model (in dB space)

Antarctic



References

- [Abreu, 2002] Abreu, R.D., Wilson, K., Arkett, M., Langlois, D., “Evaluating the use of QUIKSCAT data for operational sea ice monitoring”, IEEE IGARSS, Vol.5, pp.3032 – 3033, 2002.
- [Agnew, 2003] Agnew, T., Howell, S., “The use of operational ice charts for evaluating passive microwave ice concentration data”, Atmosphere-Ocean 41 (4), 317-331, 2003.
- [Anderson, 2005] Anderson, H.S., Long, D.G., “Sea ice mapping method for SeaWinds”, IEEE TGRS, Vol.43, No.3, 2005.
- [ASAR, 2007] European Space Agency, ‘EnviSat ASAR Product Handbook’, Issue 2.2, 2007. http://envisat.esa.int/pub/ESA_DOC/ENVISAT/ASAR/asar.ProductHandbook.2.2.pdf
- [Cavalieri, 2004] Cavalieri, D., and J. Comiso, “AMSR-E/Aqua Daily L3 12.5 km Tb, Sea Ice Conc., & Snow Depth Polar Grids V001”, March to June 2004. Boulder, CO, USA: National Snow and Ice Data Center. Digital media, 2004.
- [Cavalieri, 2006] Cavalieri, D.J., Markus, T., Hall, D.K., Gasiewski, A.J., Klein, M., Ivanoff, A., “Assessment of EOS Aqua AMSR-E Arctic sea ice concentrations using LANDSAT-7 and airborne microwave imagery”, IEEE TGRS, Vol.44, No.11, 2006.
- [Comiso, 1984] Comiso, J.C., Zwally, H.J., “Concentration gradients and growth/decay characteristics of the seasonal ice cover”, JGR, Vol. 89, No. C5, pp. 8081-8103, 1984.
- [Dedrick, 2001] Dedrick, K.R., Partington, K., VanWoert, M., Bertoia, C., Benner, D., “US National / Naval Ice Center digital sea ice and climatology data”, Canadian Journal of Remote Sensing, Vol.27, No.5, 2001.
- [Draper, 2004] Draper, D.W., Long, D.G., “Evaluating the effect of rain on SeaWinds scatterometer measurements”, JGR, Vol. 109, 2004.

- [Early, 1997] Early, D.S., Long, D.G., “Azimuthal modulation of C-Band scatterometer σ_0 over southern ocean sea ice”, IEEE TGRS, Vol.35, No.5, 1997.
- [Ezraty, 2001] Ezraty, R., Piolle, J.F., “Seawinds on Polar Sea Ice Grids: User Manual”, CONVECTION Report No.5, 2001.
- [Fernandez, 2006] Fernandez, D.E., Carswell, J.R., Frasier, S., Chang, P.S., Black, P.G., Marks, F.D., “Dual-polarized C- and Ku-band backscatter response to hurricane-force winds”, JGR, Vol.111, C08013, 2006.
- [Gohin, 1994] Gohin, F., Cavanie, A., “A first try at identification of sea ice using the three beam scatterometer of ERS-1”, Int. J. Remote Sensing, Vol.15, No.6, pp 1221-1228, 1994.
- [de Haan, 2001] de Haan, S., Stoffelen, A., “Ice discrimination using ERS scatterometer”, OSI SAF Document KNMI-TEC-TN-120, EUMETSAT, 2001.
- [Haarpaintner, 2004] Haarpaintner, J., Tonboe, R., Long, D., Van Woert, M.L., “Automatic detection and validity of the sea ice edge: an application of enhanced resolution QUIKSCAT/SeaWinds data”, IEEE TGRS, Vol.42, No.7, 2004.
- [Heinrichs, 2006] Heinrichs, J.F., Cavalieri, D.J., Markus, T., “Assessment of the AMSR sea ice concentration product at the ice edge using RADARSAT-1 and MODIS imagery”, IEEE TGRS, Vol.44, No.11, 2006.
- [Johnson, 1994] Johnson, N.L., Kotz, S., Balakrishnan, N., “Continuous univariate distributions”, Wiley, New York, 1994.
- [Jones, 1977] Jones, W.L., Schroeder, L.C., Mitchell, J.L., “Aircraft measurements of the microwave scattering signature of the ocean”, IEEE Antennas & Propagation, Vol.25, No.1, 1977.
- [de Kloe, 2007] de Kloe, J., Portabella, M., Stoffelen, A., Verhoef, A., Verspeek, J., Vogelzang, J., “SDP User Manual and Reference Guide”, NWP SAF Document KN-UD-002, EUMETSAT, 2007

- [Leidner, 2000] Leidner, S.M., Hoffman, R.N., Augenbaum, J., “Seawinds Scatterometer real-time BUFR geophysical product”, NOAA/NESDIS, 2000.
- [Markus, 2000] Markus, T., Cavalieri, D., “An enhancement of the NASA Team sea ice algorithm”, IEEE TGRS, 38: 1387-1398, 2000.
- [Markus, 2002] Markus, T., Dokken, S., “Evaluation of late summer passive microwave Arctic sea ice retrievals”, IEEE TGRS, Vol.40, No.2, 2002.
- [Meier, 2005] Meier, W.N., “A comparison of passive microwave ice concentration algorithm retrievals with AVHRR imagery in Arctic peripheral seas”, IEEE TGRS, Vol.43, No.6, 2005.
- [Meier, 2006] Meier, W.N., Fetterer, F., Fowler, C., Clemente-Colon, P., Street, T., “Operational sea ice charts: an integrated data product suitable for observing long term changes in Arctic sea ice?”, AGU Fall Meeting, 2006.
- [Meier, 2008] Meier, W.N., Stroeve, J., “Comparison of sea ice extent and ice-edge location estimates from passive microwave and enhanced resolution scatterometer data”, Ann. Glaciology, No.48, 2008.
- [Onstott, 1987] Onstott, R.G., Grenfell, T.C., Matzler, C., Luther, C.A., Svendsen, E.A., “Evolution of microwave sea ice signatures during early summer and midsummer in the Marginal Ice Zone”, JGR, Vol.92, No.C7, 1987.
- [Portabella, 2006] Portabella, M., Stoffelen, A., “Scatterometer backscatter uncertainty due to wind variability”, IEEE TGRS, Vol.44, No.11, 2006.
- [Remund, 1998] Remund, Q.P., Long, D.G., “Sea ice mapping algorithm for QuikSCAT and Seawinds”, IEEE IGARSS, pp. 1686-1688, 1998
- [Remund, 1999] Remund, Q.P., Long, D.G., “Sea ice extent mapping using Ku-band scatterometer data”, JGR, Vol.104, No.C5, pp 11,515-11,527, 1999.
- [Remund, 2000] Remund, Q.P., Long, D.G., “Iterative estimation of Antarctic sea ice extent using Seawinds data”, IEEE IGARSS, pp. 491-493, 2000.

- [Remund, 2003] Remund, Q.P., Long, D.G., “Large scale inverse Ku-Band backscatter modeling of sea ice”, IEEE TGRS, Vol.41, No.8, 2003.
- [Riggs, 1999] Riggs, G. A., D. K. Hall, and S. A. Ackerman, “Sea ice extent and classification mapping with the Moderate Resolution Imaging Spectro-Radiometer Airborne Simulator” Remote Sensing of the Environment 68:152-163, 1999.
- [Spencer, 2000] Spencer, M.K., Chianlin, W., Long, D.G., “Improved resolution backscatter measurements with the Seawinds pencil-beam scatterometer”, IEEE TGRS, Vol.38, No.1, 2000.
- [Stoffelen, 2006] Stoffelen, A., Portabella, M., “On bayesian scatterometer wind inversion”, IEEE TGRS, Vol.44, No.6, 2006.
- [Verspeek, 2006] Verspeek, J.A., “Sea ice classification using Bayesian statistics”, KNMI Internal Report, 2006.
- [Wentz, 1999] Wentz, F.J., Smith, D.K., “A model function for the normalized radar cross-section at 14GHz derived from NSCAT observations”, JGR, Vol.104, N.C5, pp. 11499-11514, 1999.
- [Worby, 2004] Worby, A.P., Comiso, J.C., “Studies of the Antarctic sea ice edge and ice extent from satellite and ship observations”, Remote Sensing Environment, No. 92, pp. 98-111, 2004.
- [Yueh, 1997] Yueh, S.H., Kwok, R., Lou, S.H., Tsai, W.Y., “Sea ice identification using dual polarized Ku-Band data”, IEEE TGRS, Vol.35, No.3, 1997.

Acknowledgements

We acknowledge the collaboration of our colleagues in the scatterometer group at KNMI. Special mention goes to Anton Verhoef and Jeroen Verspeek for their timely contributions. This work is funded by the European Meteorological Satellite Organization (EUMETSAT) Ocean & Sea Ice (OSI) Satellite Application Facilities (SAF).